SELF-SUSTAINED COMBUSTION OF LOW GRADE SOLID FUELS IN A STAGNATION-POINT REVERSE-FLOW COMBUSTOR

A Dissertation
Presented to
The Academic Faculty

by

Arun Radhakrishnan

In Partial Fulfillment
of the Requirements for the Degree
Doctor of Philosophy in the
School of Aerospace Engineering

Georgia Institute of Technology
December 2013

SELF-SUSTAINED COMBUSTION OF LOW GRADE SOLID FUELS IN A STAGNATION-POINT REVERSE-FLOW COMBUSTOR

Approved by:

Dr. Jerry M. Seitzman, Advisor
Professor
School of Aerospace Engineering
Georgia Institute of Technology

Dr. Ben T. Zinn
Regents Professor
School of Aerospace Engineering
Georgia Institute of Technology

Dr. Carsten Sievers, Dr. rer. nat.
Assistant Professor
School of Chemical & Biomolecular
Engineering
Georgia Institute of Technology

Dr. Timothy C. Lieuwen
Professor
School of Aerospace Engineering
Georgia Institute of Technology

Dr. Jechiel J. Jagoda
Professor, Associate Chair for Graduate
Studies and Research
School of Aerospace Engineering
Georgia Institute of Technology

Date Approved:

To my parents ...

ACKNOWLEDGEMENTS

I would, first and foremost, like to acknowledge the contribution of my advisor, Dr. Jerry M. Seitzman towards my thesis. His in-depth knowledge of subject matter, extensive research experience and exemplary leadership qualities have all been of immense benefit towards the timely completion of this research project.

Next, I would like to express my most sincere gratitude to my undergraduate mentor, Dr. R.I. Sujith. I learned a lot of data analysis and literature review methods under his able guidance. I would also like to thank Dr. Mohan Bobba for providing me with an opportunity to assist him with his research work. This served to enhance my grasp of various experimental techniques and proper research etiquette. Further, the contribution of Mr. James Cornacchio towards development of experimental facilities deserves special mention.

Lastly, I would like to honor the contribution of my friends at different stages of this work. Worthy of mention among them are Messers Yash Kochar, Sampath Adusumili, Ben Wilde and Tom Slais. The interest and help they have provided has been extremely instrumental in keeping me motivated throughout my graduate career.

TABLE OF CONTENTS

LIST OF FIGURES

LIST OF TABLES

SUMMARY

This thesis investigates the use of the Stagnation-Point Reverse-Flow (SPRF) combustor geometry for burning low-grade solid fuels that are attractive for specific industrial applications because of their low cost and on-site availability. These fuels are in general, hard to burn, either because of high moisture and impurity-content, e.g. biomass, or their low-volatiles content, e.g., petroleum-coke. This results in various challenges to the combustor designer, for example reduced flame stability and poor combustion efficiency. Conventional solutions include preheating the incoming flow as well as co-firing with high-grade fuels. The SPRF combustor geometry has been chosen because it was demonstrated to operate stably on standard gaseous and liquid-fuels corresponding to ultra fuel-lean conditions and power densities at atmospheric-pressure around 20-25 MW/m^3. Previous studies on the SPRF combustor have proven that the unique, reverse flow-geometry allows entrainment of near-adiabatic products into the incoming reactants, thereby enhancing the reactivity of the mixture. Further, the presence of the stagnation-end created a region of low mean velocities and high levels of unsteadiness and mixing-rates that supported the reaction-zones. In this study, we examine the performance of the SPRF geometry on a specific low grade solid fuel, petroleum coke.

There are three main goals of this thesis. The first goal is the design of a SPRF combustor to operate on solid-fuels based on a design-scaling methodology, as well as demonstration of successful operation corresponding to a baseline condition. The second goal involves understanding the mode of operation of the SPRF combustor on solid-fuels based on visualization studies. The third goal of this thesis is developing and using reduced-order models to better understand and predict the ignition and quasi-steady burning behavior of dispersed-phase particles in the SPRF combustor.

The SPRF combustor has been demonstrated to operate stably on pure-oxygen and a slurry made from water and petroleum-coke, both at the baseline conditions (125 kW, 18 g/s, ~25 μm particles) and higher power-densities and powder sizes. For an overall combustor length less than a meter, combustion is not complete (global combustion efficiency less than 70%). Luminance imaging results indicate the incoming reactant jet ignites and exhibits intense burning at the mid-combustor region, around 15 jet diameters downstream of the inlet, most likely due to enhanced mixing as a result of the highly unsteady velocity field. This roughly corresponds to the location of the reaction zones in the previous SPRF combustors operating on gas and liquid fuels. Planar laser visualization of the reacting flow-field using particle-scattering reveals that ignition of a significant amount of the reactants occurs only after the incoming jet has broken into reactant packets. Post-ignition, these burning packets burn out slowly as they reverse direction and exit the combustor on either side of the central injector. This is unlike the behavior in liquid and gas-fueled operation where the incoming reactants burned across a highly corrugated, thin-flame front. Based on these findings, as well as the results of previous SPRF studies, an idealized model of combustor operation based on a plug flow reactor has been developed. The predictions suggest that fuel-conversion efficiency is enhanced by the combustor operating pressure and lowered by the heat-losses.

Overall, this effort has shown the SPRF geometry is a promising compact-combustor concept for self-sustained operation on low-grade solid-fuels for typical high-pressure applications such as direct steam-generation. Based on these findings, it is recommended that future designs for the specific application previously mentioned have a shorter base-combustor with lower heat-losses and a longer steam-generation section for injection of water.

CHAPTER 1

INTRODUCTION AND MOTIVATION

1.1   Introduction

In practical combustors, the phase of the fuel strongly affects the ease of combustion, especially in the case of gaseous oxidizers[1]. Arguably, liquid fuels are harder to burn than gaseous fuels as the net burning rates are limited by the vaporization and mixing processes in the surrounding gas phase oxidizer. In the case of liquid fuels with very high boiling points, the gas-phase reaction shifts almost entirely to the surface. This behavior is similar to that of solid fuels like carbon and aluminum where the particles can burn predominantly through attack of oxygen on the surface and to a lesser extent through the oxidation of the volatile content evolved from the surface[2]. In short, these fuels are harder to burn than gaseous fuels or even low-boiling-point liquid fuels like gasoline or Jet-A.

Practical carbonaceous solid fuels contain varied proportion of volatile matter and impurities and thus can be classified into different grades[3]. In general, the lower the grade, lower the extent of combustible volatile matter and higher the extent of impurities. While no specific distinction exists, some of the industrial fuels like petroleum-coke or biomass are classified into "low-grade" category and are especially attractive because of cost-effectiveness or simplicity of combustor design.

The most commonly used solid fuel in industrial combustion systems is coal. The standard approaches for burning coal are fixed bed, circulating bed and pulverized-coal combustion systems, The distinction between these three classes of combustion systems is primarily based on the fuel-feed techniques and thus the mode of heat-feedback and combustion [4]. In comparison with the fixed and circulating bed systems, the pulverized-coal systems burn

relatively fine particles in oxidizer at near stoichiometric conditions. Consequently, the power density and operating temperature is higher in comparison with the fixed bed and entrained bed systems. However, the higher NO_x and fly-ash emissions associated with pulverized-coal systems render it unsuitable for certain applications. With the development of efficient scrubbers, pulverized combustion technology is being increasingly preferred for most coal-burning applications.

To enhance product feedback and thus statically stable combustor operation, pulverized coal burners utilize swirling flow, a bluff body and a quarl geometry to create a central recirculation zone [5]. As a consequence, significant heat-release occurs only after a portion of the incoming particles are ignited by the re-circulating hot-products. This acts to stabilize the remaining combustion process. Problems occur if this central recirculation zone results in too little entrainment or insufficient residence time, resulting in loss of static stability. Typically, the incoming gases are preheated to temperatures of up to 1000 K to move the ignition location closer to the burner, thereby resulting in more compact, stable flames [6]. However, this approach poses challenges in the form of coal-dust explosions and added hardware in the form of heat-exchangers. Recent studies have demonstrated that geometry improvements also have a significant effect on the extent of product entrainment and thus static stability. Bluff-body based swirl-burners [7] force the ignition point closer to the quarl and make stable operation possible at O_2 concentrations as low as 18.0%, with a lower oxygen concentration important for exhaust gas recirculation (EGR) systems.

Significant operational challenges, including static stability and fuel-conversion efficiency, exist when retrofitting coal-burning combustors to operate on low-grade solid-fuels. Circulating bed and pulverized combustion systems have been adapted to burn low grade fuels

2

[8-11]. In most cases, additional design changes were required, including extensive preheating and co-firing with superior fuels, e.g., coal.

A recently developed approach, the Stagnation Point Reverse Flow (SPRF) combustor geometry, has been shown to have some unique attributes favored for good performance with low-grade fuels. Previous studies [12] have shown that the SPRF combustor can operate stably on superior gaseous and liquid-fuels over a large range of conditions. These include ultra fuel-lean conditions close to the flammability limits of the fuels used, while providing high power densities (20 MW/m^3). Non-intrusive diagnostic studies [13] have proven that the unique reverse flow-geometry allows entrainment of near-adiabatic products into the reactants (essentially internal EGR), thereby enhancing the reactivity of the incoming mixture. Further, the presence of the stagnation end creates a region of low mean velocities and high levels of unsteadiness and mixing-rates that supported the reaction-zones.
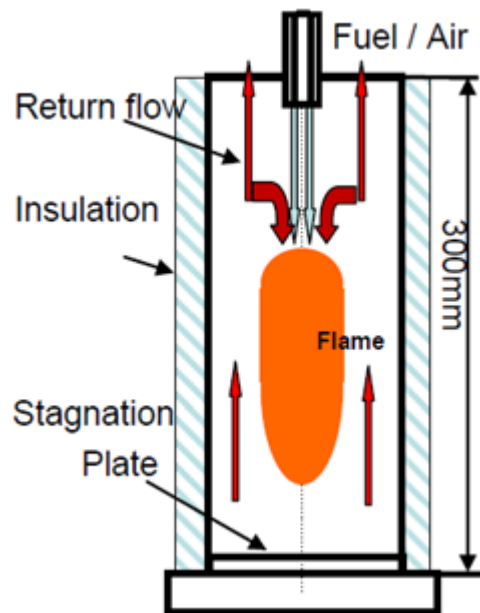
Figure 1. Schematic of a SPRF combustor that burned liquid and gaseous fuels.

3

There are a variety of potential uses for the SPRF system for high power density combustion of solid fuels; a motivating case for this work is steam generation. In general, the generated steam could be either through indirect process involving heat-exchangers or through direct injection of water into the products of combustion. Presumably, the "indirect" technique produces relatively cleaner steam and is therefore the preferred mode in power generation using turbines. In comparison, the "direct" steam generation process has lower hardware costs and less stringent requirement on water-quality although it produces relatively impure steam fouled with particulates and gaseous combustion products.

Recently, the direct steam-generation (DSG) technique has attracted much attention because of its potential applications in thermal extraction processes used in mining and oil industry faced with the challenges of escalating costs involved with the process. DSG for oil recovery operations is commercially implemented using either Steam Simulation process (CSS) and the Steam Assisted Gravity Drainage (SAGD) process [14, 15]. These processes are usually very energy intensive and often require high-pressure steam, devoid of diluents like nitrogen. Consequently, higher operating pressures, pure oxygen as oxidizer and cheaper fuels are preferred design and feed parameters for the steam generator operation. A commonly used readily available fuel for the oil industry is petroleum coke, commonly known as pet-coke, a by-product of the refining process primarily composed of carbon (a typical chemical composition is given in Table 1). Previous studies [16] utilized a twin-atomizer based quarl-burner for high intensity combustion of pet-coke slurry in co-flowing air.

Table 1. Results of analysis of petroleum-coke composition commonly used in oil industry

PROXIMATE ANALYSIS	
QUANTITY	DRY WEIGHT (%)
Volatiles	12.0
Fixed Carbon	81.0
Ash	0.4
ULTIMATE ANALYSIS	
QUANTITY	WEIGHT (%)
Moisture	0.2
Ash	0.4
Carbon	84.6
Hydrogen	4.0
Nitrogen	2.0
Oxygen	2.8
Sulfur	6.0

1.2   Thesis Objective

Previous studies on SPRF have been conducted on gas and liquid fuels, mostly corresponding to a single baseline geometry. Clearly, the design for slow-burning fuels as petroleum,-coke for given baseline operating power requires the capability to scale the designs based on these previous SPRF studies. Further, there is also the need to characterize the performance and understand the mechanism of operation. Such results would help improve the design for potential applications in high-pressure direct steam generation, as described in Section 1.1.

1.3   Overview of the Present Work

Based on the discussion in Section 1.2, it is possible to outline three main tasks, namely: (1) development of a SPRF combustor scaled based on the previous designs for operation on

solid fuels and performance characterization corresponding to different operating conditions, (2) characterization of combustion and flow-field characteristics that contribute to the static stability of combustion process and (3) development of the capability to predict performance corresponding to different operating conditions.

Chapter 2 presents the literature survey of the background relevant to SPRF studies, combustion of solid fuel and the development of the scaling methodology. Chapter 3 describes the experimental methods including setup and the development of numerical methods to model the ignition and quasi-steady burning of particles. Chapter 4 describes the performance of the SPRF combustor and the results of predictions of the idealized model corresponding to variations in operating conditions. Chapter 5 describes the results of visualization studies on the reacting flow-field and the predictions of the numerical model to understand the static stability mechanism of the combustor. Lastly, conclusions and suggestions for future research are presented in Chapter 6.

CHAPTER 2

BACKGROUND AND MODEL DEVELOPMENT

This chapter provides the necessary background on concepts relevant to understand the data analysis approaches and the results presented in the following chapters. As introduced in the previous chapter, this thesis involves investigation of the SPRF combustion technology for burning low-grade, solid fuels. Consequently, this chapter has two main sections:- the first section on the understanding of background on the flow and combustion processes in the SPRF configuration based on previous work with gaseous and liquid fuels, and background the second section on the properties and combustion behavior of solid fuels in relation to their combustion characteristics. The SPRF background, namely Section 2.1 describes three main issues, namely previous studies on the SPRF velocity field, the reaction zone locations and the product-reactant mixing.

In Section 2.2, individual and group combustion behaviors of solid particles are presented along with a discussion on the results of previous studies on surface kinetic rates of individual particles. This section concludes with a discussion on a discussion on the various paradigms to analyze inter-particle effects on the group-combustion of multiple particles dispersed in a gas-phase oxidizer. Lastly, Section 2.3 details the formulation of design-methodology of a generic prototype SPRF combustor for baseline-operation of choice, based on important findings from the previous SPRF studies as well as combustion behavior of solid-fuels.

2.1   SPRF Combustor Studies

2.1.1   Combustor Geometry

As described in Chapter 1, the central-injection SPRF combustor consists of an injector positioned centrally within a tube that is open at one end and closed at the other. Most of the studies have been performed on a single liquid and gas-fueled central-injection SPRF geometry corresponding to pre-mixed as well as non-premixed introduction of fuel and air. In the non-premixed operation, the fuel was injected through an inner tube within the main-injector and air through the annular space between the fuel-tube and the main-injector, as shown in Figure 2(a) (gas-operation) and Figure 2(b) (liquid-operation). For the gas-fueled premixed operation, the fuel and air were premixed upstream of the main injector in the injector side-inlet and the inner-tube was blocked-off to prevent entrainment of the ambient-air. In comparison, for the liquid-fueled premixed case, the inner fuel-tube was retracted within the main-injector resulting in good-dispersion of the fuel droplets in the co-flowing air, as shown in Figure 2(c)
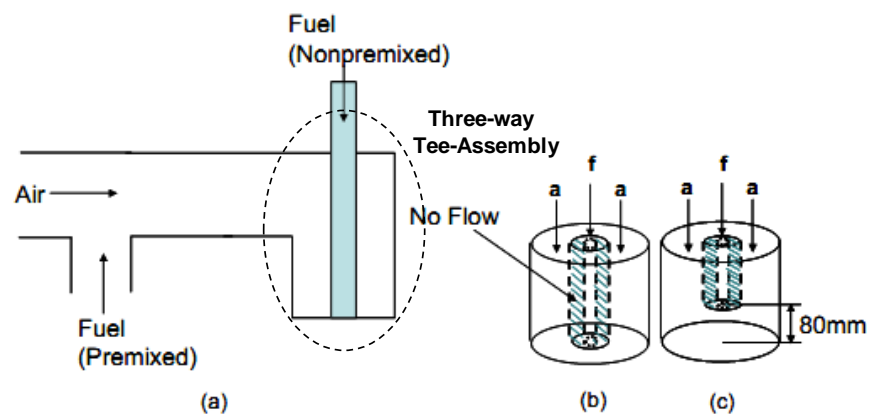
Figure 2. Schematic of the injectors used for: (a) Gas-fueled operation; and for liquid-fueled operation in a (b) Flush-configuration and (c) Retracted-configuration.

9

The cylindrical SPRF combustor-tube is made of fused-quartz and is open at both ends. The inner-diameter of this tube is 70mm and the overall length is 300 mm. One of the two open-ends is seated snugly inside a circular groove cut into a base-plate such that there is no measurable leakage of fuel/air through the groove. The base-plate region contained within the SPRF-tube serves to act as a closed-end for the combustor and has provision for embedding a quartz-disk so as to allow the laser-sheet for diagnostics to enter the combustor.

As a consequence of reactant-injection into a tube closed at one end, the flow stagnates, reverses direction and exits through the open-end. Presumably, this stagnation-location is characterized by low-mean velocities and high levels of unsteadiness resulting in high mixing rates between the incoming and return fluid-packets. Additionally, the shear between the incoming and return flow results in further mixing between the two-streams as well as deceleration of the incoming –flow. Conceivably, heat-addition can affect and be in turn affected by the flow-field, altering the mean flow-velocities, the unsteadiness levels and thus the mixing rates. The following sub-sections give a detailed description of quantitative studies on velocity field, product mixing as well as spatially resolved visualization of the reacting flow-field.

2.1.2 Velocity Field

The velocity-field of the SPRF combustor operating with gaseous inflows was has been measured using the Particle Image Velocimetry (PIV) technique[17]. Studies were performed for non-reacting conditions, as well as for combustion with the fuel and air entering either for pre-mixed and or non-premixed introduction of the reactants[17, 18]. The main features of the flow-field are elucidated by first reviewing the non-reacting case followed by a discussion on the effect of heat-release. In the configuration studied, reactants were injected centrally through an inner tube positioned in the open end, while the return-flow exited through the open end through

10

the annular region between the combustor tube wall and the inner central injector tube, as seen in Figure 2. As evident from in the mean axial velocity profile shown in Figure 4 (a), the shear between the incoming jet and the counter-flowing products was shown to decelerate the reactant jet. This resulted in stagnation and subsequent flow-reversal of the incoming jet. Close to the stagnation region, the two shear-layers merged, resulting in high overall values of the turbulent-velocity fluctuations (u'_{rms}/u') (Figure 4(b)). This region is also characterized by low-mean velocities (U) and consequently high levels of turbulence intensity ($u'_{rms} u''/U$) resulting in higher unsteadiness and mixing rates between the incoming and return flow (Figure 4(c)).

Next we review the previous studies to determine the effect of heat release on the velocity-field beginning with a through a comparison of the mean axial velocities in the reacting and the non-reacting cases. The measurements obtained in that work (see Figure 5(a)), showed that the injection velocities, namely the centerline mean axial velocity at the injector exit, are were generally higher because of reactant preheating within the injector by exiting products. Downstream of the injection location, the incoming flow decelerates due to the effect of shear in the reacting case similar to the non-reacting case. However, heat release and the subsequent ensuing volumetric expansion of product gases reduces the net deceleration of the incoming flow in the reacting case. This is evident from the fact that the centerline mean velocity exhibits a less-steep decay rate, and consequently, the flow stagnates farther downstream for the reacting case.
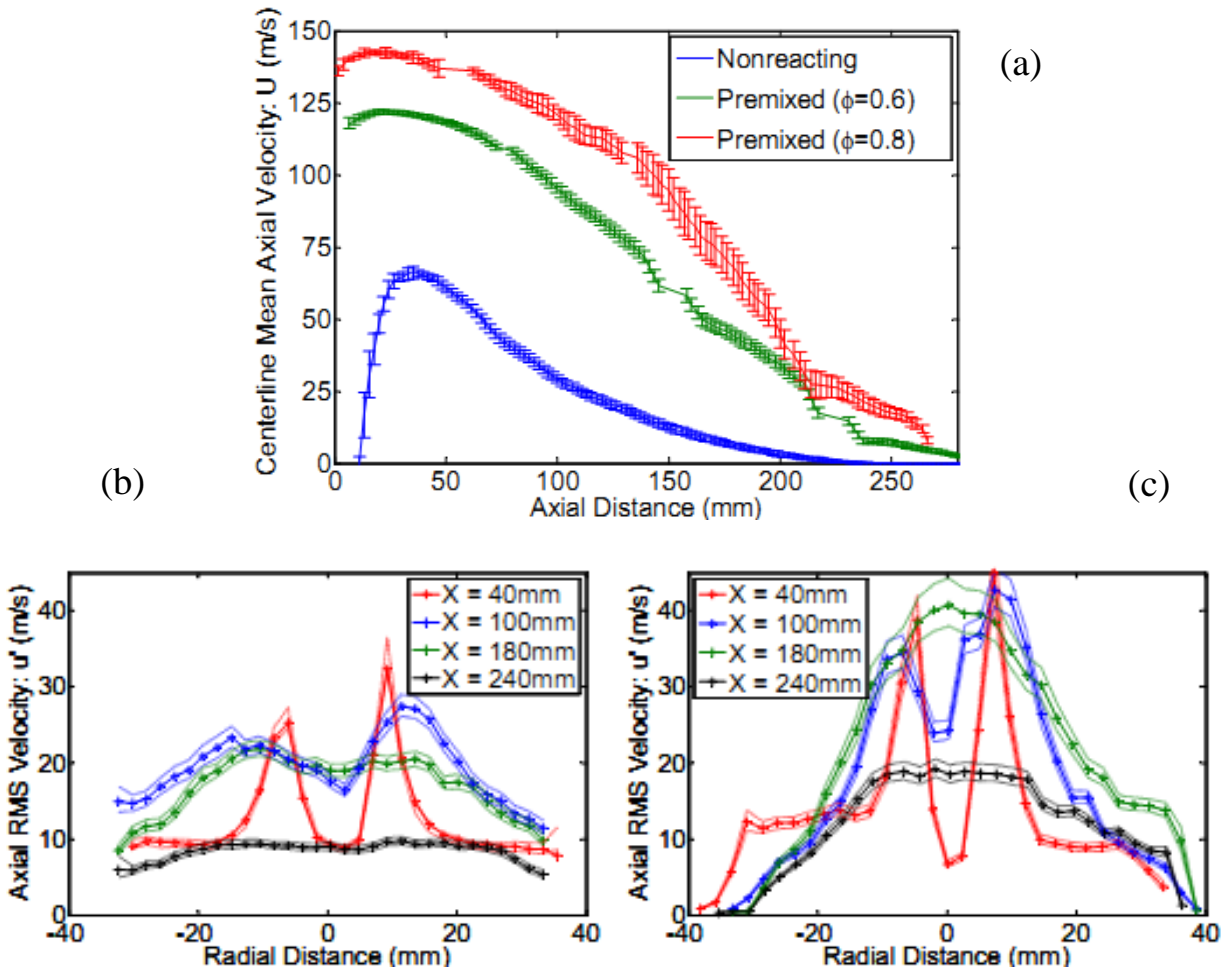
Figure 3.Heat release effects on SPRF Flow-field: (a) centerline mean axial velocity variation and radial profiles of axial RMS velocity for reacting cases - (b) premixed, Φ=0.6

Similar to the mean centerline flow-field, the measured shear-layer thickness and the overall unsteadiness of the flow-field were also altered as a result of heat release. In general, the presence of heat-release was found to cause thinner and longer shear-layers as well as higher levels of unsteadiness in the velocity field. Further, the axial velocity fluctuations and turbulence intensities appear to be positively correlated with the extent of heat-release, as seen in Figure 6. This is evident from comparison of the plots showing higher values for the aforementioned quantities corresponding to the case having a higher fuel-air ratio, namely Figure 6 (b) and (c), which compare two fuel-air ratio cases (Φ=0.6 and 0.8) than Figure 5(b) (Φ=0.6).
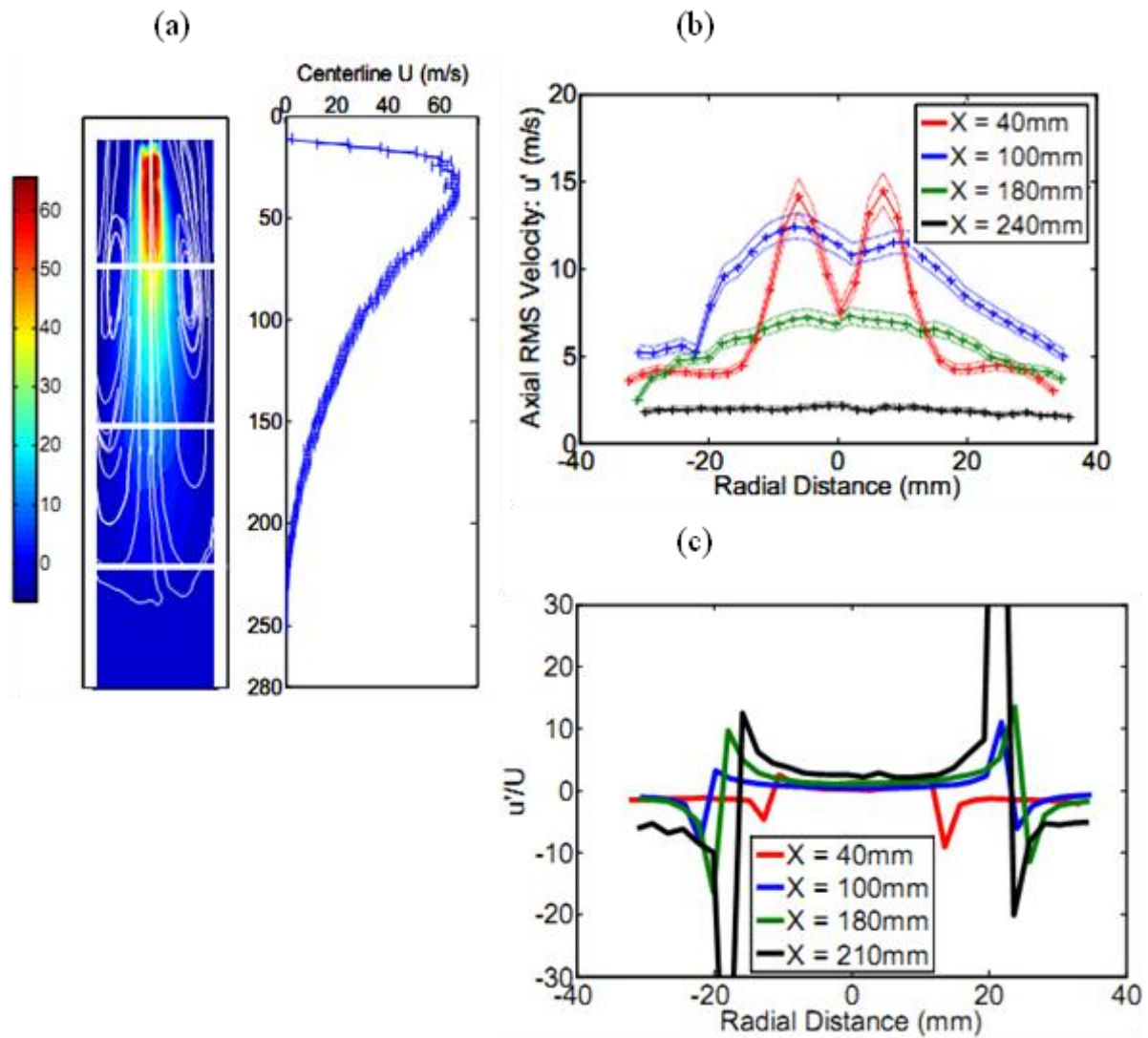
Figure 4.Non-reacting SPRF Flow-field: (a) centerline mean axial velocity variation, (b) radial profiles of axial RMS velocity (non-reacting case) and (c) radial profiles of axial u'/U [1].
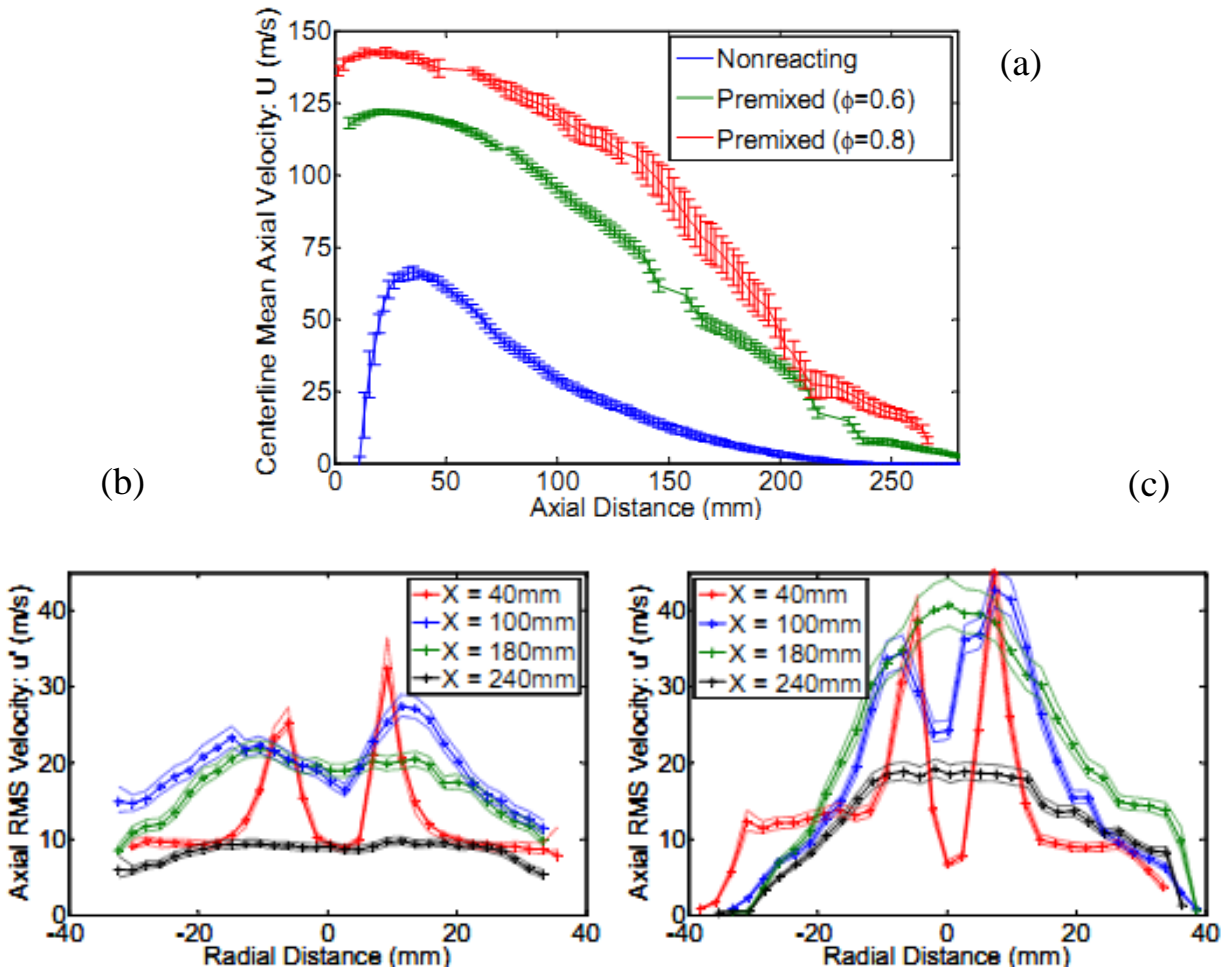
Figure 5.Heat release effects on SPRF Flow-field: (a) centerline mean axial velocity variation and radial profiles of axial RMS velocity for reacting cases - (b) premixed, Φ=0.6 and (c) premixed, Φ=0.8

The high levels of unsteadiness produced due to by the heat release result in are characterized by significantly higher flapping motions of the reactant jet in the reacting case (b) Figure (a), as compared to the non-reacting case Figure 6(a) in the second and third quarter regions of the combustor. In that work [19], it was suggested that on an instantaneous basis, the reactant jet is deformed, pushed out of plane and occasionally broken into reactant packets. These interpretations were confirmed by 3-dimensional CFD [17] results like those shown in

Figure 6(c). An example of the CFD axial velocity contours, obtained which were calculated for the same inlet conditions as the PIV-data, is included in Figure 6(c).
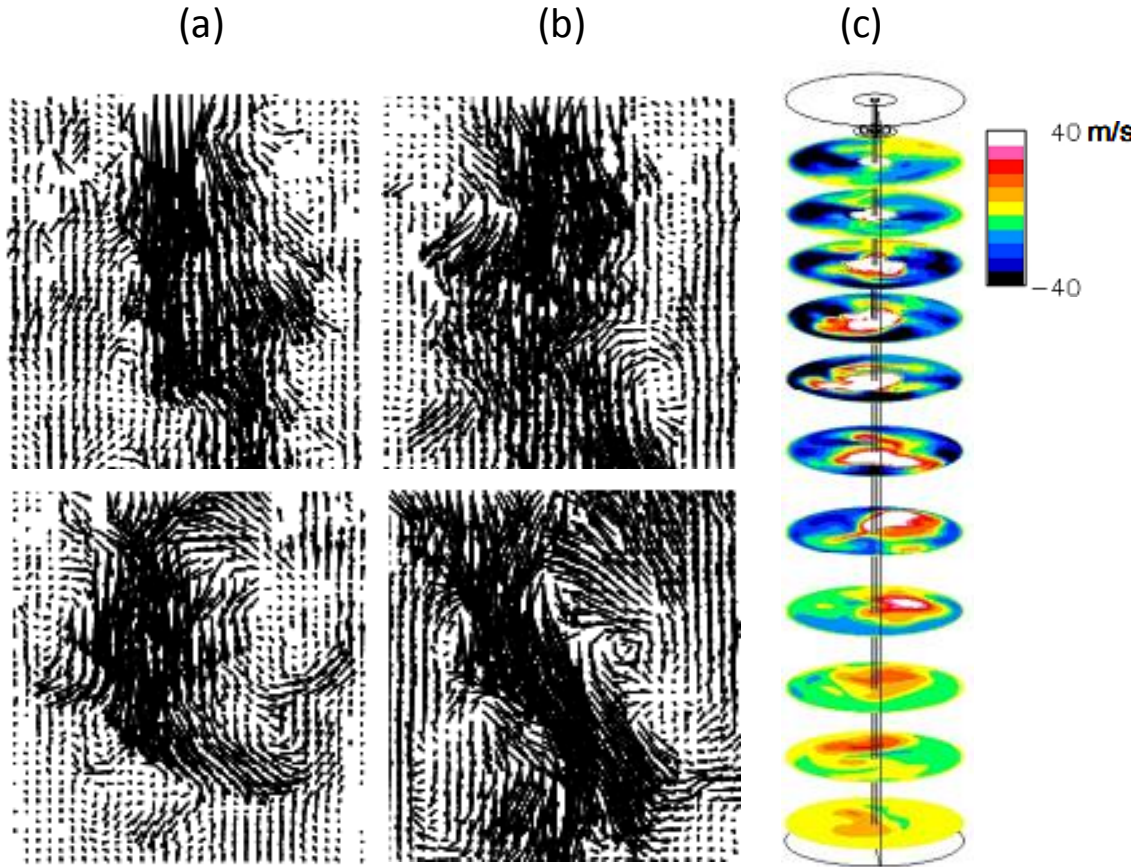
Figure 6. Instantaneous SPRF flow-field (a) 2nd and 3rd quarter, non-reacting, (b) 2nd and 3rd quarter, reacting and (c) 3-D axial velocity contours (computational data), reacting

2.1.3 Reaction Zone Visualization

The results from chemiluminescence imaging have been used to identify the location of reaction zones in the SPRF combustor operating on gaseous and liquid fuels [20, 21]. As described in sub-section 2.1.1, the flush-injector geometry facilitated the authors to study the effect of non-premixed injection on the combustion characteristics of liquid-fueled SPRF combustor. Further in liquid-fueled operation, two fuel injector locations were studied: a

15

retracted case and a flush case. The effect of premixing was partially simulated by retracting the liquid fuel tube within the air-injector. In the flush case, the liquid-fuel tube was in the same plane as the exit of the air-injector; thus it is similar to the non-premixed gas-combustor case.

As shown in Figure 6(a), the average chemiluminescence image for premixed (gas-fueled) operation revealed the presence of a weak, nearly attached reaction zone, with the majority of the reaction spread between the second and third quarters of the combustor length.
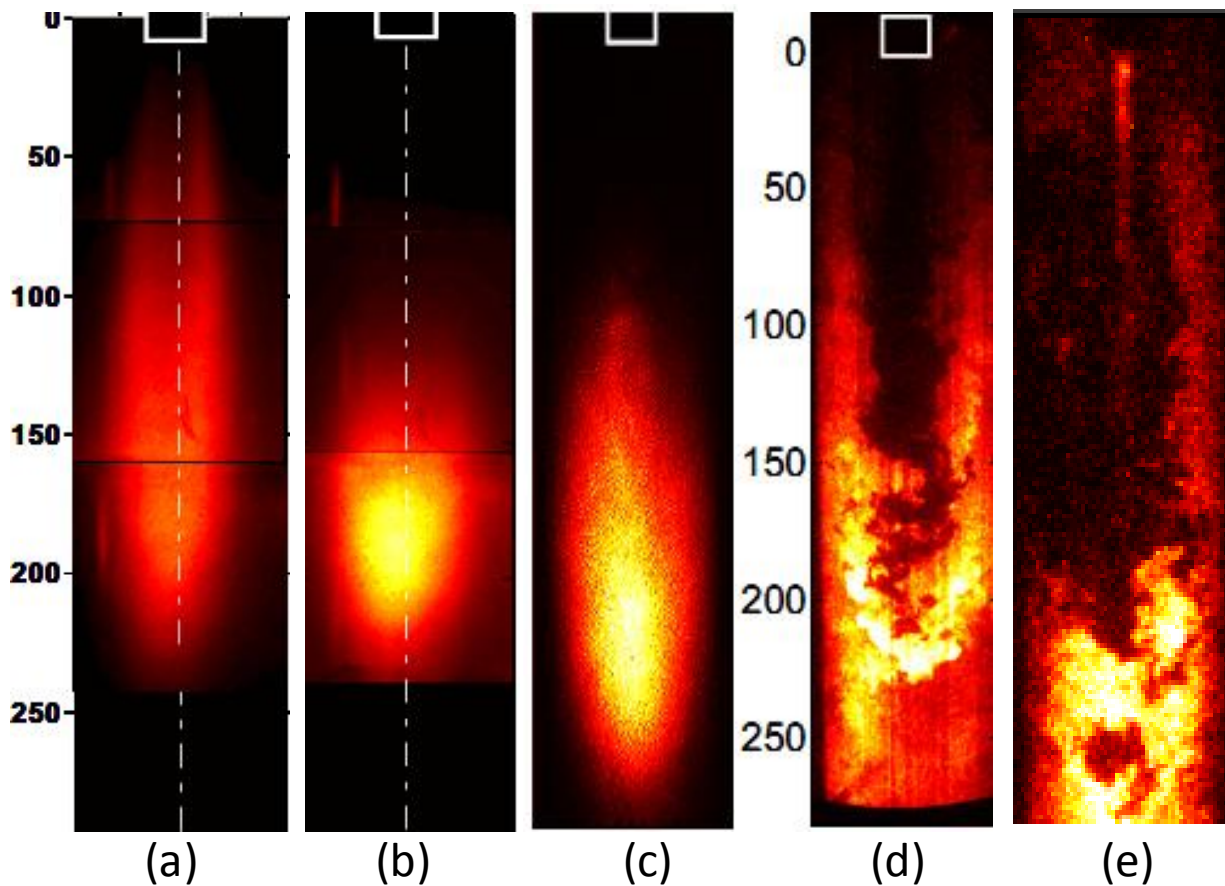
Figure 6 . SPRF reacting flow-field visualization: chemiluminescence imaging for: (a) gas, premixed (b) gas, non-premixed, (c) liquid, flush-injection and OH-PLIF imaging for: (d) gas, non-premixed and (e) liquid-flush injection

Whereas in the non-premixed case shown in Figure 6(b), there was no measureable heat-release close to the injector; the flame was stabilized entirely in the third-quarter region. This is the region of low axial velocities and high turbulence intensities, as described previously. In addition, the lift-off length was found to increase with the momentum of the incoming jet. Similarly, when operated on liquid fuel with a flush-injector Figure 6(c), the time-averaged reaction zones occurred in roughly the same spatial location as for the non-premixed, gas-fueled combustor.

The spatially resolved, instantaneous structure of the reaction zones was also studied using the OH PLIF technique for the gas- and liquid- fueled SPRF combustors [19, 20]. Figure 6(d) and Figure 6(e) show example instantaneous OH PLIF images for the non-premixed (gas) and flush (liquid) cases. Analysis of large sets of such images revealed that the reactant jets often break into packets in the highly turbulent, low velocity region (third quarter). In addition, the gas- and liquid-fueled combustors contained highly corrugated, thin-flame fronts.

2.1.4 Product Mixing Studies

As evident from the planar OH PLIF images, the lack of a flame (consistently) attached to the SPRF injector allows for products to be entrained into the reactant jet before the reactants burn. The importance of hot product entrainment into the incoming reactants was studied using Spontaneous Raman Scattering (SRS) measurements of the major species concentrations for the gas-fueled SPRF combustor [22]. The extent of product entrainment was quantified using a product-fraction parameter, f_p, defined as the ratio of the mass-fraction of products to that of the reactants.

As a combined result of intermittent entrainment and turbulent motion, the f_p values fluctuate in time. To exclude instances corresponding to an unmixed product packet within the

17

SRS probe volume, the authors applied conditional sampling; instantaneous cases where the fuel-fraction was below a particular threshold level were considered to be pure product packets and were eliminated from the calculation of mixing statistics. Corresponding to the baseline-injector results shown in Figure 7, product-entrainment starts as early as X/D of 4.0 characterized by f_p values of greater than zero and attains a maximum-value of around 0.8 before the reactants reach the flame, at an X/D of approximately 12.0.
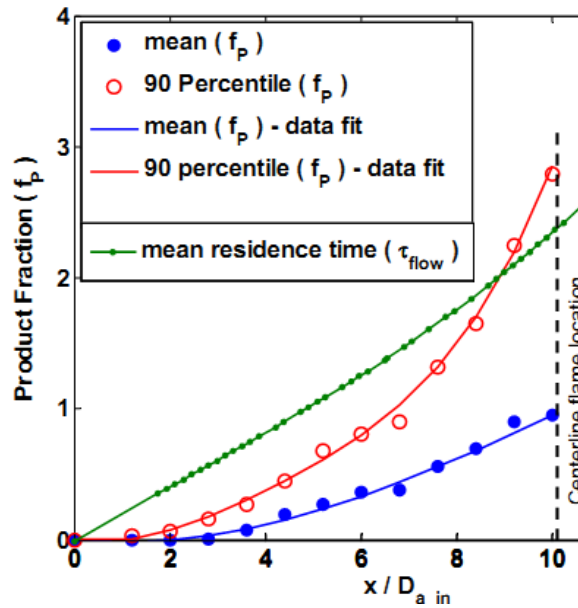
Figure 7. Axial variation of mean and 90 percentile product-fractions along the premixed combustor centerline.

As a combined result of intermittent entrainment and turbulent motion, the f_p values fluctuate in time. To exclude instances corresponding to an unmixed product packet within the SRS probe volume, the authors applied conditional sampling; instantaneous cases where the fuel-fraction was below a particular threshold level were considered to be pure product packets and were eliminated from the calculation of mixing statistics. As seen in Figure 7, the average

centerline f_p attains a value of around 0.8 before the reactants reach the flame corresponding to an X/D of approximately 10.0.
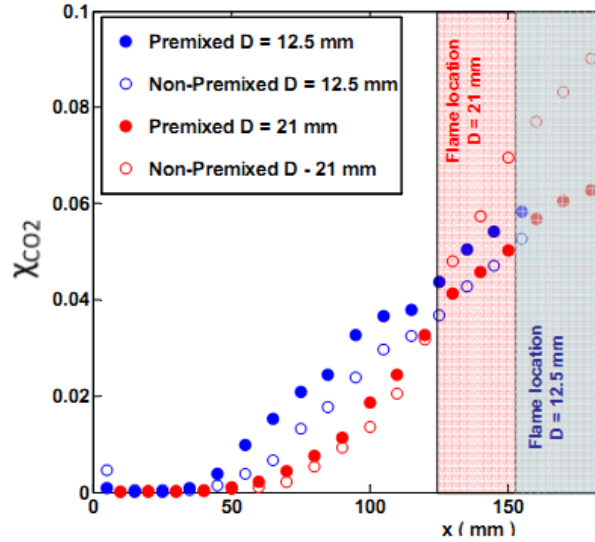
Figure 8. Effect of injection velocity on mean CO2 mole-fraction along combustor centerline for premixed and non-premixed modes of operation.

The extent of product entrainment in the SPRF combustor was also shown to be dependent on the relative momentum of the incoming jet. Figure 8 compares the measured centerline f_p values for two injector tubes of differing diameters and injection velocities for the same overall flow rates. Results are shown for premixed and non-premixed operation. For both cases, the wider tube, with a lower incoming momentum, was found to entrain lesser products than the higher momentum injector.

2.1.5 Summary

As observed by the authors, most of the heat-release for the non-premixed SPRF operation on gas as well as liquid-fuels occurs in the lower-half of the combustor. This region, in particular, is characterized by high levels of unsteadiness (u_{rms}') and thus higher mixing-rates between the incoming and the return-flow. The authors concluded that in the gas-fueled

operation, this large stand-off distance allowed sufficient time for the fuel and air to mix as well as the incoming reactants to entrain sufficient amount of products resulting in a preheated, diluted mixture prior to combustion. Further, it has also been reported that in liquid-fueled operation, preheating of the incoming reactants due to product entrainment results in vaporization and mixing of the atomized liquid jet in the co-flowing mixture, prior to reaching the flame zones. As observed by the authors, the incoming preheated and diluted mixture burned as thin, highly corrugated flames in the region characterized by high unsteadiness levels corresponding to both gas as well as liquid-fueled operation.

Further, it has also been reported that product-entrainment starts close to the injector, i.e. the measured level (f_p) rises from zero as early as X/D of 4.0 until the maximum mean-value of 0.8 at the flame-location. The authors also reported that lower injection velocities corresponding to a wider injector tube results in lower centerline mean f_p than the standard geometry. As a consequence it may be concluded that corresponding to an acceptable level of pressure-loss in the injector, it is important to have higher velocities in order to have higher entrainment as well as better dispersion of the fuel in the co-flowing oxidizer jet.

2.2   Combustion of Carbonaceous Solid Fuels

2.2.1   Single Particle Combustion

Carbonaceous solid fuels, in general, and petroleum-coke, in particular, are a heterogeneous mixture of different individual constituents of varying chemical composition and physical structure [23]. Consequently, interesting features have been observed during heating, ignition and sustained combustion of such fuels. At lower particle temperatures, the moisture content escapes as water vapor. Further heating changes the chemical and resulting in evolution of volatile gases comprised mostly of lighter hydrocarbons, hydrogen and carbon monoxide. The

20

amount of volatile matter evolved varies depending on chemical composition of the carbonaceous fuel and the heating rate, often resulting in significant changes in the physical structure like swelling, pore-formation and fragmentation of the particle [24]. The porous physical structure of these fuels allows for the leakage of evolved volatile gases to the ambient, a process commonly referred to as "devolatilization". The residual solid matter is comprised mainly of fixed carbon, commonly referred to as char, and inorganic matter, commonly referred to also known as ash.

As the evolved volatiles mix and burn homogeneously in the gaseous phase surrounding the solid particles, the associated high volumetric heat-release rates result in significant escalation of the residual particle temperature. Following complete devolatilization and combustion of volatiles, the ambient oxidizing species, primarily O_2 and to a lesser extent CO_2 and H_2O are able to diffuse to the surface and the pores of the hot particle. Subsequently the char progressively burns through reactions of oxidizing species, on the exterior and internal pore-surface, a process commonly referred to as heterogeneous combustion. Generally, heterogeneous combustion, being a surface phenomenon, is slower than the gas-phase combustion which proceeds homogeneously within a given volume. As a result, the net heterogeneous combustion rates are dependent on both the surface kinetic rate, governed by the particle temperature, as well as the rate of oxygen-diffusion to the surface of the particle.

During the initial stages of char-burning characterized by low particle temperatures, the heterogeneous combustion rate is limited by the surface kinetics. This slower combustion-phase is commonly referred to in the literature as "Zone-I" or "chemistry-limited" burning [23, 25]. With increasing particle temperature and associated surface kinetic rates, the extent of depletion of oxidizing species concentration at the surface and within the pores increases. This

intermediate burning stage is referred to as "Zone-II" combustion [23]. Generally, ignition is believed to occur between the colder Zone-I phase and the Zone-II phase characterized by higher surface kinetic-rates. At the asymptotic limit of "Zone-II" combustion, the particle temperatures reach their peak values, whereas the surface oxygen concentrations reach their minimum value. As a consequence, surface oxidation is limited by the diffusion of major oxidizing species, with limited contribution from the any internal pore-structure of the char. This limiting mode of burning is commonly referred to in the literature as "Zone-III" or "diffusion-limited" burning [23]. Depending on the relative proportion of volatiles and hence the physical structure of the char, structure of char, it is possible to have "Zone-I" burning during the ignition-phase and either "Zone-II" or "Zone-III" as could be the dominant mode of steady-state combustion. The following sub-section discusses the composition of our specific fuel, namely petroleum-coke and the impact of its composition on the burning properties.

2.2.1.1 Petroleum Coke Attributes: Composition and Combustion

As described in the first chapter, petroleum-coke has a varied composition depending on the source and characteristic processing techniques prior to usage as a fuel. Generally, in comparison with coal, petroleum-coke has lower volatile and higher fixed-carbon content. Consequently, the initial stages like devolatilization and combustion of volatiles are relatively unimportant during the combustion of petroleum-coke particles with sizes in the range of 20-100 μm, typically used in practical combustors. Further, the resulting char would be relatively devoid of significant internal pore-structure. As a result, ignition and combustion can be assumed to proceed due to reactions at the external surface, with rates governed by surface kinetics during ignition-phase (Zone-I) and by diffusional rates during the quasi-steady-combustion phase

(Zone-III). Thus the particle-density can be assumed to remain constant during the period of combustion and the burning-rate for the particle can be approximated by a "shrinking-sphere" as:

$$\dot{m} = 4\pi\rho_p r_p^2 \frac{dr_p}{dt}$$ 2.1

Experimental studies conducted by Boukara and Prado (referred to henceforth as BP-92)[26] used a drop-tube furnace, equipped with and pyrometry and laser-scattering techniques to obtain the ignition characteristics of petroleum-coke and petroleum-coke chars. Ignition probability was defined as the number of ignition events recorded by the pyrometer, normalized by the total number of particle detections recorded by the particle-scattering counter. Subsequently, a statistical Probit method was used to obtain an ignition-temperature (T_{ig}), defined as the inlet-gas temperature at which the characteristic ignition-probability curve exhibits a point of inflexion. The surface-recession rate for the "shrinking-sphere" was approximated based on an Arrhenius model, as given below:

$$\frac{dr}{dt} = A\exp\left(-\frac{E_a}{RT_p}\right)\chi_{O2,s}^a$$ 2.2

Using Semenov's theory of ignition based on the balance between the steady-state heat-production and heat-loss at the ignition-temperature (T_{ig}), Arrhenius rate- constants for surface-kinetics were obtained have been provided (see Table 2). The authors established good agreement between the experimentally measured ignition delay and the corresponding predicted values for different particle -sizes ranging from 100 to 500 μm. For the baseline case corresponding to 100 μm and a gas-temperature of 1300 K, the measured ignition delay has been measured to be close to 125 ms.

Similar studies study conducted by Smith *et al.* (referred to henceforth as S-82)[27] used a drop-tube method based on coupled pyrometry and exhaust-gas sampling technique to

23

investigate the quasi-steady combustion characteristics of petroleum-coke chars. The burning-rates, obtained by measurement of gas composition at various axial locations in the drop-tube furnace, were converted to a surface-recession rate, based on the "shrinking-sphere" assumption mentioned previously. In conjunction with the particle-temperatures measured using optical-pyrometry, the surface regression-rates were converted to Arrhenius rate-constants for surface-kinetics corresponding to the quasi-steady combustion phase. These values provided in Table 2 have been used for the determination of characteristic ignition delay and the steady-state combustion of petroleum-coke char in our combustor. Further details of development of the model are described in the following section.

Table 2. Arrhenius surface-kinetic rate constants of petroleum-coke chars experimentally determined for ignition-phase (BP-92 study)[26] and quasi-steady combustion-phase (S-82 study)[27].

Combustion-Phase	A (m/s)	Ea (kJ)	a
Ignition (Boukara, Prado)	42050	94.0	1.0
Steady-State (Smith)	3050	42.8	1.0

2.2.1.2 <u>Characteristic Ignition Temperature</u>

To successfully burn particles in a compact combustor with a limited residence time, it is important to achieve relatively fast ignition such that sufficient time remains for the particles to burn before exiting the combustor. Evidently, the ignition delay corresponding to the baseline case of the BP-92 study is significantly greater than the residence time of 30 ms, reported earlier corresponding to the SPRF baseline operating conditions. As a consequence, particle-ignition

and thus self-sustained combustion is possible within the SPRF geometry only corresponding to higher gas-temperatures. Therefore it is useful to define a "characteristic ignition temperature" ($T_{ig,c}$) for a specific particle size, as the gas-temperature at which the predicted ignition delay is lesser than the actual combustor residence-time by a factor (f). Mathematically this can be expressed as:

$$T_{ig,c} = T_g \mid_{\tau_{ig} < f \tau_{SPRF,res}} \qquad 2.3$$

As most of the SPRF results presented earlier are for methane-air combustion, it is helpful to compare the behavior of petroleum-coke to methane. Figure 9 shows the predicted ignition delay for a 50 μm pet coke particle as a function of ambient air-temperature for a single petroleum-coke particle. This figure also includes the auto-ignition temperatures for methane corresponding to a stoichiometric methane-air mixture. The pet coke results are based on the kinetic rates presented in Table 2, while the methane-air values were calculated with CHEMKIN software and the GRIMech - 3.0 reaction mechanism [28]. The results show that methane has higher apparent effective activation energy, as evidenced by the ignition delay for methane exhibiting a sharper drop with gas-temperature as compared to the 50 μm petroleum-coke particle.

For sufficiently long allowable times, the pet coke can be ignited by lower temperatures compared to the auto-ignition temperature of methane. For short times, however, pet coke is harder to ignite. For example at 10 ms, the characteristic ignition temperature for petroleum - coke is (1450 K), which is higher than that of for methane (1280 K). This indicates pet-coke combustion will require higher operating temperatures and/or longer residence times compared to the previous SPRF systems.
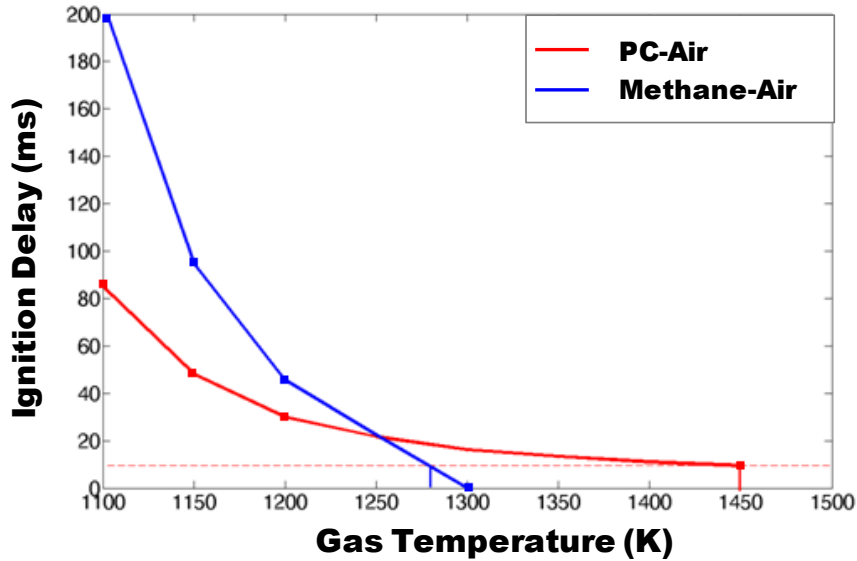
Figure 9. Comparison of temperature dependence of predicted ignition-delays of: (a)50 μm petroleum-coke (red) particle in air and (b) stoichiometric methane-air mixture (blue).

2.2.2 Group Combustion Paradigms

The previous sub-section described the combustion processes of a single carbonaceous solid-particle in a quiescent infinite ambient. However, in practical combustion devices, a large number of the pulverized particles are typically dispersed in the surrounding gaseous environment, say an O_2/diluent mixture. Consequently the combustion of a single particle affects and in turn is affected by other particles in its neighborhood through radiative transfer of energy and inter-particle exchange of boundary-layer gas surrounding the particle [23]. This inter-particle exchange could be dominated either by gaseous conduction or turbulent transport depending on the level of unsteadiness of the flow-field.

Studies conducted on conical-flame burners [29, 30] have revealed that at low levels of unsteadiness, the reaction zone essentially has the character of a laminar dust-flame front propagating into reactants. Excellent correlation was observed between results of analytical dust-

26

flame models derived analogous to a laminar premixed gas-flame front and experimentally measured dust-flame speed values.
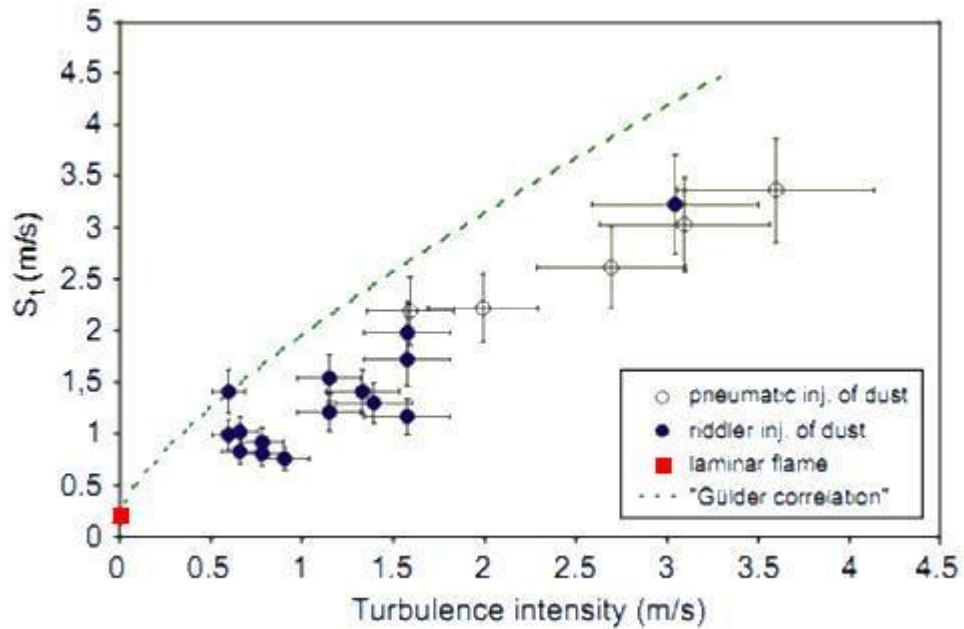
Figure 10. Correlation between turbulent burning velocity and turbulence intensity for gel-dust, a carbonaceous solid. (SP-07 study)[31].

Similar studies were conducted by Schneider and Proust[31] (referred to hence forth as SP-07) on freely propagating dust-flame fronts subjected to varying levels of turbulence intensity (u'_{rms}). At low turbulence levels, the captured images of reaction zones have revealed the presence of increased burning area. It is believed that the generated eddies wrinkle the laminar dust-flame front similar to a laminar gas-flame front, although the physics has not been completely understood. At higher turbulence levels, it is believed that the eddies are able to wrap around particles resulting in a breakdown in the dust-flame structure. Conceivably, the interfacial region between the reactants and burning products start to resemble a distributed reaction zone. Irrespective of the different regimes, the SP-07 study established that the turbulent burning velocities and the turbulence intensity are positively correlated (Figure 10). Thus it may be

concluded that turbulent transport is the dominant mechanism responsible for the static stability of combustion process in high mixing regions of practical combustors like Circulating Fluidized Bed reactors or Entrained Flow reactors.

2.3 SPRF Scaling Methodology Formulation

Based on the discussion in Section 2.1, it is clear that many features of the SPRF geometry enable operation corresponding to non-premixed introduction of fuel and oxidizer or air with good mixture preparation prior to reaching reaction zones. In this section, we utilize the results of visualization and product-mixing studies on gas and liquid fueled baseline SPRF presented earlier to formulate scaling methodology for a generic combustion system based on the SPRF geometry.

As described earlier, the SPRF performance is highly dependent on the injection velocities and to a lesser extent on the combustor dimensions for the gas-fueled SPRF operation. Generally, higher injection velocities are beneficial for higher better dispersion of fuel in the co-flowing oxidizer stream as well as better mixing between the incoming reactants and returning products. However, higher injection pressure losses force a tradeoff in the choice of injection velocity. Previous SPRF injector studies confirmed that the characteristic pressure drop is lesser than 5% of the total pressure corresponding to baseline operation. Corresponding to this injection velocity, products constituted approximately 70% of the total reactant mixture. Therefore the baseline SPRF injection velocity is roughly taken as the injection velocity for our proposed pet-coke SPRF combustor configuration. The injector area for the generic combustion system is derived from the corresponding mass flow-rates and the injection velocities. These rules have can be represented by:

$$A_{injector,generic} = A_{injector,baselineSPRF} \left(\frac{\dot{m}_{ox,generic}}{\dot{m}_{ox,baseline\,SPRF}} \right) \left(\frac{\rho_{ox,baseline\,SPRF}}{\rho_{ox,generic}} \right) \qquad 2.4$$

As the combustor tube-diameter was found to have a less significant effect on the product entrainment than the injection velocity [32], it is intuitive to use somewhat larger diameter tubes for the petroleum-coke SPRF generic system designs. This design concept would increase the overall residence times for complete combustion of the fuel, without noticeably degrading the reactant-product mixing.

CHAPTER 3

EXPERIMENTAL AND MODELING METHODS

This chapter describes the tools and techniques used in this work to meet the goals outlined in the first chapter. Section 3.1 describes the experimental approach and various methods employed. Specifically, the SPRF combustor configurations developed for burning pet coke, and the various sub-systems of the flow facility are detailed. This is followed by a description of the layout of the imaging and laser-diagnostic systems. The section concludes with a discussion on the various procedures adopted to analyze and interpret data as well as convert them into parameters of interest.

Section 3.2 details the methods adopted to model the basic performance of the SPRF combustor for burning of solids. The methods are based on the particle burning concepts that were introduced in Chapter 2. Specifically, the simplifying assumptions and numerical tools applied to solve the governing equations in order to model the various processes within the combustor are discussed.

3.1   Experimental Methods

3.1.1   Experimental Setup

The layout of the combustor and various sub-systems of the experimental setup, namely: (i) the reactant feed-system, (ii) the exhaust-sampling and analysis system, and (iii) the exhaust-cleanup system are shown in Figure 11. Two separate laboratory-scale atmospheric-pressure combustors have been used for this work, denoted as the *prototype combustor* and the *visualization combustor*. The prototype combustor version was designed and constructed to

minimize heat-losses and to enable testing for extended periods of time. The visualization combustor, though similar in geometry to the prototype combustor, was designed with modifications primarily to provide optical access for visualization studies. The common features of these designs include the co-annular injector positioned centrally within the combustor and the pilot-module at the base for igniting the reactants.

The reactant feed-system supplies the fuel, namely petroleum-coke, and the oxidizer, namely gaseous oxygen, to the injector. As introduced in Chapter 1, one motivation for this work was is eventual application of the prototype combustor for steam-generation at high pressure. Thus, a wet feed-system (i.e., slurry) was chosen for transport of the fuel. The slurry approach, as compared to a dry feed system, is well-suited for constant feed-rate injection at high pressure. The injection of water with the solid fuel is also compatible with the intended steam-generation application, and it provides the capability of accurate metering of flow-rates at high operating pressures. The exhaust from the combustor is sampled immediately downstream of the combustor exit and analyzed for the composition using the exhaust-sampling and analysis system. Prior to venting into the building exhaust, the combustion products are processed using an exhaust-cleanup system based on a venturi wet-scrubber. The following sub-sections describe the combustor and the various sub-systems in detail.
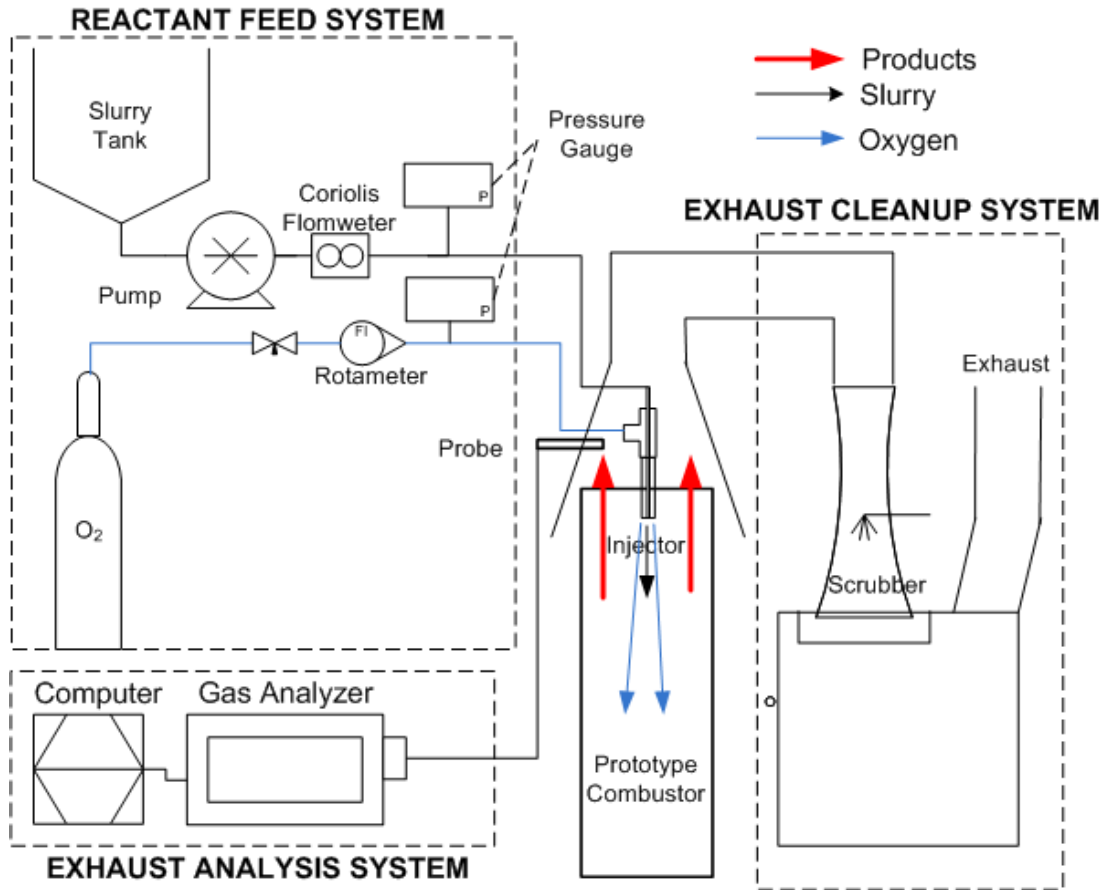
Figure 11. Experimental layout of the prototype combustor and various sub-systems used for this work

3.1.1.1 Combustor Construction

Based on the previous SPRF studies, a scaling methodology for combustor and injector design was formulated in Chapter 2 in order to ensure statically stable operation with good fuel-conversion efficiency. Essentially the combustor was scaled based on the central injection SPRF geometry such that the dimensions were higher in order to increase the residence time for complete combustion of slow-burning fuels like petroleum-coke. Table 3 compares the approximate dimensions of the prototype combustor and the baseline central-injection SPRF geometry. Presumably, with a lesser relative change in width in comparison with that of the

length, the jet confinement is not affected resulting in better mixing between the incoming jet and the return products.

The actual prototype combustor, however, is modular in construction - consisting of the base-combustor, an added burnout section and a pilot-module, as shown in Figure 12. The construction of the base combustor and burnout section is similar. Both of them consist of two steel pipes (with I.D. of 120 mm) cooled externally by a water jacket and lined with a high temperature coating of zirconium oxide (heat resistant to 2500 K), 6.25 mm thick and cast directly into each of the sections. The resulting combustor inner-diameter (ID), after correcting for the thickness of the high-temperature of zirconium-oxide, is around 108 mm and is closer to the value recommended by the design-scaling methodology (Table 3).

The pilot or the igniter module consists of a chamber with separate ports for fuel (Φ=9.5 mm) and air (Φ=6.25 mm). The pilot module screws into the bottom section of the base-combustor. Impinging jets of fuel and air, as shown in Figure 12, stabilize a non-premixed pilot flame downstream of the chamber exit for igniting the spray injected centrally from the top end.

The visualization-combustor consists of a cylindrical tube (GE fused quartz), 460 mm long, seated inside a circular slot cut-out into a stainless-steel base-plate, as shown in Figure 13. Three pre-cast zirconia cylindrical insulators (114 mm OD $\times$ 102 mm ID) are stacked inside the quartz tube in order to minimize heat losses and damage to the quartz tube due to high combustion temperatures. The lowest zirconia insulator is seated snugly into a circular slot cut-out into the base-plate and concentric with the outer-slot.

Table 3. Comparison of the dimensions of the baseline SPRF (actual) and baseline prototype-combustor (recommended).

	Combustor Dimensions	
	Central Injection SPRF	Prototype Combustor
Width (W; in mm)	76.2	95 (Recommended)
Length (L; in mm)	279.4	419 (Recommended)
Recommended ΔW (%)	-	25.0
Recommended ΔL (%)	-	50.0

One of the three zirconia tubes has two side-slots, 6 mm wide, located diametrically opposite to each other and a cut-out that subtends an angle of 115° with the central axis of the combustor. The side-slots provide optical access for a laser sheet and the cut-out forms an optical-window for viewing a portion of the reacting flow-field. The relative position of the windowed-insulator can be changed in the stack to visualize different axial regions of the combustor. The clearance between the full ceramic cylinders, i.e., the ones without the cut-out, and the quartz tube is sealed with ceramic-padding to lessen any leakage of gases into the annular space.
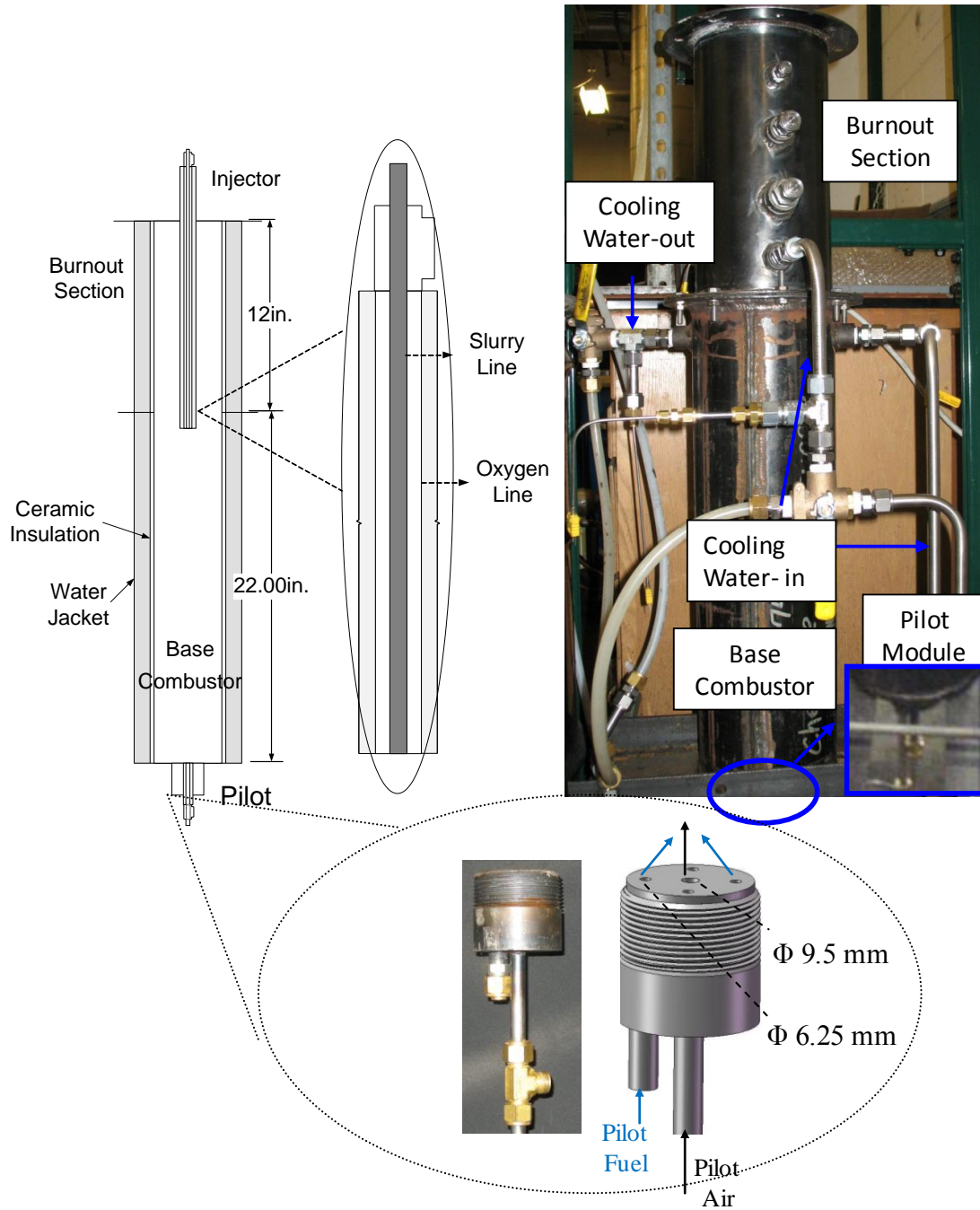
Figure 12. Detailed layout of the prototype combustor and coaxial injector used for this work
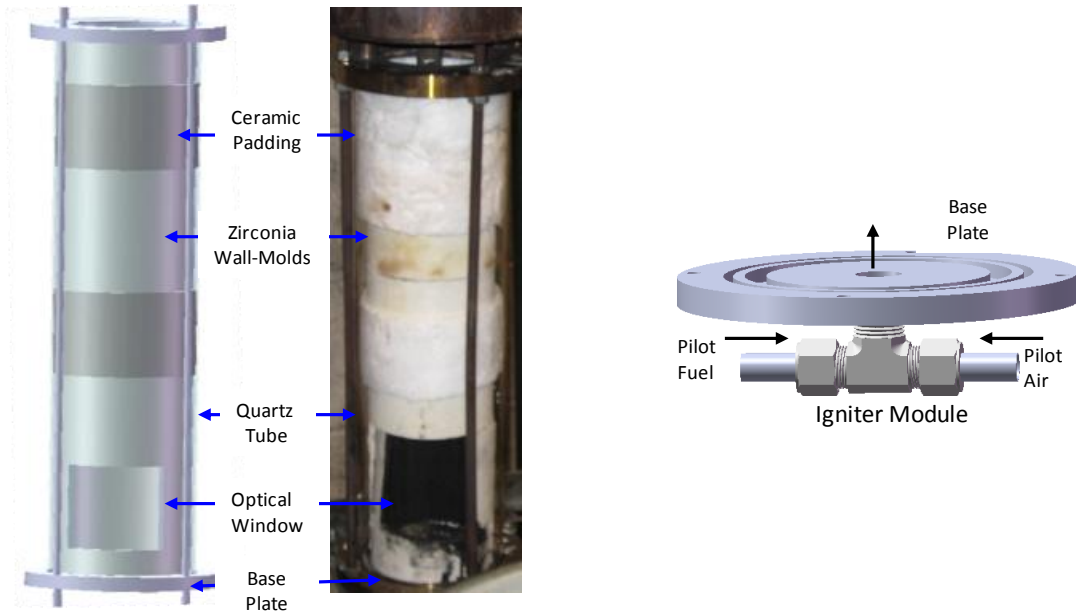
Figure 13. Detailed layout of the visualization along with photograph (left) and the igniter design (right)

3.1.1.2 Injector

In this part of the sub-section on experimental-setup, we utilize the scaling methodology formulated in Chapter 2 for the design of injector. Table 4 compares the various baseline parameters of the prototype combustor and the central-injection SPRF geometry and recommends an injector area of ~0.80 cm². The actual co-annular injector construction consists of an inner metal tube (4.76 mm OD × 3.2 mm ID) positioned centrally within an outer tube (12.5 mm OD × 10 mm ID) with the help of three set screws. This design provides a net-injector area of 0.607 cm² which is close to the value recommended by the use of scaling methodology described in Chapter 2.

This simple atomizer is based on a previous central-injection SPRF operating on liquid fuel with a flush injector design [21]. However, the inner-diameter (ID) of the inner tube is higher larger in order to reduce instances of clogging due to agglomerating particles. The outer

metal tube is coated with a 6 mm thick Zirconia layer cast directly onto the surface. The inner tube transports slurry into the combustor, and the slurry is atomized by the high velocity oxygen jet flowing through the annular space between the two tubes. The injector extends approximately 50 mm into the base-combustor section of the prototype combustor as well as the visualization combustor.

Table 4. Comparison of the injector dimensions of the central-injection SPRF (actual) and the prototype-combustor (recommended).

	Baseline Operation	
	Central Injection SPRF	Prototype Combustor
Operating Power (kW)	12.8	125
Equivalence-Ratio (Φ)	0.58	1.0
Oxidizer Flow Rate (g/s)	7.8	10.2
Oxidizer Density (kg/m^3)	0.836	1.3
Injector Area (mm^2)	94.7	79.6 (Recommended)

3.1.1.3 Reactant Feed-System

A steady, regulated supply of gaseous oxygen is fed to the injector from compressed gas-bottles through oil-free supply lines and metered with a calibrated rotameter (RMC-106-SPCL-VIT). The wet-feed system supplies a steady flow-rate of pressurized slurry into the injector. The slurry is made by mixing pulverized petroleum-coke and water in the ratio 1:1 by weight and stabilized by a surfactant, Triton X-114, which comprises 1.0% by weight of the slurry. The six-stage progressive-cavity pump (Moyno 6M2CDQAAA) draws in a steady flow-rate of slurry

stored in a 30-gallon container, relatively independent of the obstruction in the pump-outlet for operating pressures up to 300 psi. The flow rate of the cavity pump is adjusted using a frequency controller that changes the rotational speed of the pump and is measured using a coriolis flow meter (Micromotion R025S114NDAEZZZ).

3.1.1.4 Exhaust Sampling and Analysis System

Coal consists of high percentage of volatile, typically 30-40 % by weight. As the extent of devolatilization varies depending on the combustor residence time, detailed elemental char analysis is the preferred technique for measurement of combustion efficiency [33, 34]. For solid fuels like petroleum-coke with lower volatiles and higher combustion temperature, it is likely that the entire volatile matter is evolved during the combustion process. Thus, the errors associated with the relatively simple exhaust sampling technique should be low enough to render it effective in comparison with the detailed elemental analysis technique.

The composition of the exhaust gas is continuously monitored and recorded using by a Horiba CEMS-PG 250 gas-analyzer Horiba CEMS-PG 250 (designated "Horiba", for short throughout this thesis), and the Horiba is connected to a computer through a data-acquisition interface for continuous recording of the results. As seen in Figure 14, the gas-analyzer has a built-in suction pump to draw in gases through a water-cooled sampling probe sheathed by ceramic tube for extractive sampling. The Horiba analyzer uses various measurements techniques like non-dispersive IR for the CO_2 measurement and an electrochemical cell for the O_2 measurements. The analyzer is calibrated periodically against a standard set of gases of known composition for accuracy of 0.5% full-scale.

Because of the non-linear nature of the response of the measurement technique sensors at higher CO_2 and O_2 mole-fractions, as well as interference from H_2O, the extracted sample is

38

diluted and dried prior to analysis. The dilution gas is high-purity nitrogen, which is mixed with the gas-sample in the ratio 4:1 by volume, i.e., four parts by volume of N_2 for every one part by volume of exhaust gases. As evidenced from the measurements of gas-composition in the following chapter, the highest CO mole-fractions recorded are below 500 ppm, after correcting for the effects of dilution and drying. As a consequence, Equation 3.1 provided below can be used for calculation of the instantaneous global fuel-conversion efficiency.

$$\eta_{fuel} = \frac{0.928 \left(\dfrac{\chi_{CO_2,measured}}{\chi_{O_2,measured}} \right) + 0.00829}{\left(\dfrac{\chi_{CO_2,measured}}{\chi_{O_2,measured}} \right) + 1} \qquad 3.1$$
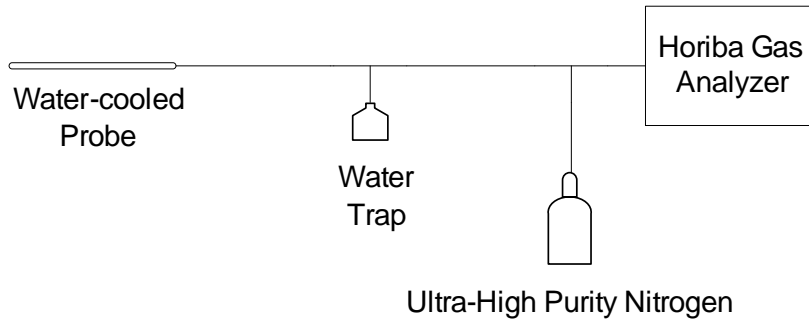
Figure 14. Layout of the setup used for extractive sampling and analysis of exhaust-gases from the combustor-exit

3.1.1.5 Exhaust Cleanup System

A steady, high-velocity water spray within a venturi wet-scrubber unit cleans the exhaust gases of ash and unburned-particles. The use of proper additives like caustic-soda and oxidizing chemicals also helps clean the exhaust of toxic-pollutants like H_2S, SO_2 and Volatile Organic Compounds (VOC) before release into the atmosphere. The entrainment-effect due to the high

velocity spray further augments the drafting effect produced by the negative pressures in the system because of the building exhaust. The wet-scrubber unit has a sudden converging section to accelerate the gases and thereby increase the rates of ash and unburned-particle deposition within droplets as well as a gradual diverging section downstream of the throat that helps in pressure-recovery. The droplets and bigger particles, characterized by higher inertia, collect in the drum whereas the scrubbed gases are vented into the building exhaust.

3.1.2   Visualization Techniques

This section details the various techniques adopted to visualize the reacting flow-field of the combustor as well as characterize the injector performance. The first sub-section describes the optical layout of the simultaneous particle-scattering and luminance imaging setup used for flow-field visualization. The statistics of the spray, namely the mean agglomerate sizes produced by the co-annular injector in un-confined tests, have been are measured using spray-atomization studies, as described in the second sub-section.

3.1.2.1 <u>Particle-Scattering Imaging</u>

The optical-setup for imaging of particles within the reacting flow-field (shown in Figure 15) consists of: (i) an illumination source, (ii) sheet-forming optics and (iii) an imaging-system. The illumination-source is a laser beam generated from the 2nd harmonic output (532 nm) of a dual-head, Q-switched Nd:YAG laser (Surelite I-10). The laser-beam is expanded into a planar laser sheet approximately 75 mm wide and 300 μm thick, using a set of 3 fused silica lenses. The laser repetition rate is 10 Hz with pulse energy of 95 mJ/pulse. Since the pulse is very short (FWHM=8 ns), it effectively freezes the flow, up to supersonic velocities. The imaging system consists of a laser-line filter with peak-transmittance at 532 nm and FWHM of 10 nm positioned in front of a UV-Nikkor lens (105 mm f/4.0) coupled to an intensified CCD camera (PI-MAX

512×X512). The scattered light camera is synchronized with the laser-head such that the Q-switch turns on the laser-pulse within the short ICCD exposure-duration of 100 ns.

The luminance-signal from hot, glowing particles is captured simultaneously with the particle-scattering signal using an imaging system that forms a part of the particle-scattering setup, as shown in Figure 15. The imaging-system consists of a set of two optical-filters positioned in front of a Nikkor lens (55 mm, f/2.8) coupled to a CCD camera (Foculus FO531SB, 1800×X1200 pixels). The filters, namely an ND filter (transmittance=0.33) and a 2 mm thick blue-green BG-18 filter (320-660 nm) reduce background-radiation from the ceramic insulation material. The camera is triggered by the laser such that the CCD detector starts acquiring images 20 μs after the reacting flow-field has been illuminated by the laser-sheet. Thus nearly simultaneous imaging is possible with minimal interference of the captured luminance signal from elastic laser-scattering. The luminance camera is aligned with the particle-scattering camera such that the angle between them is as small as possible and their fields of view are matched to include the entire length and width of the imaging window.
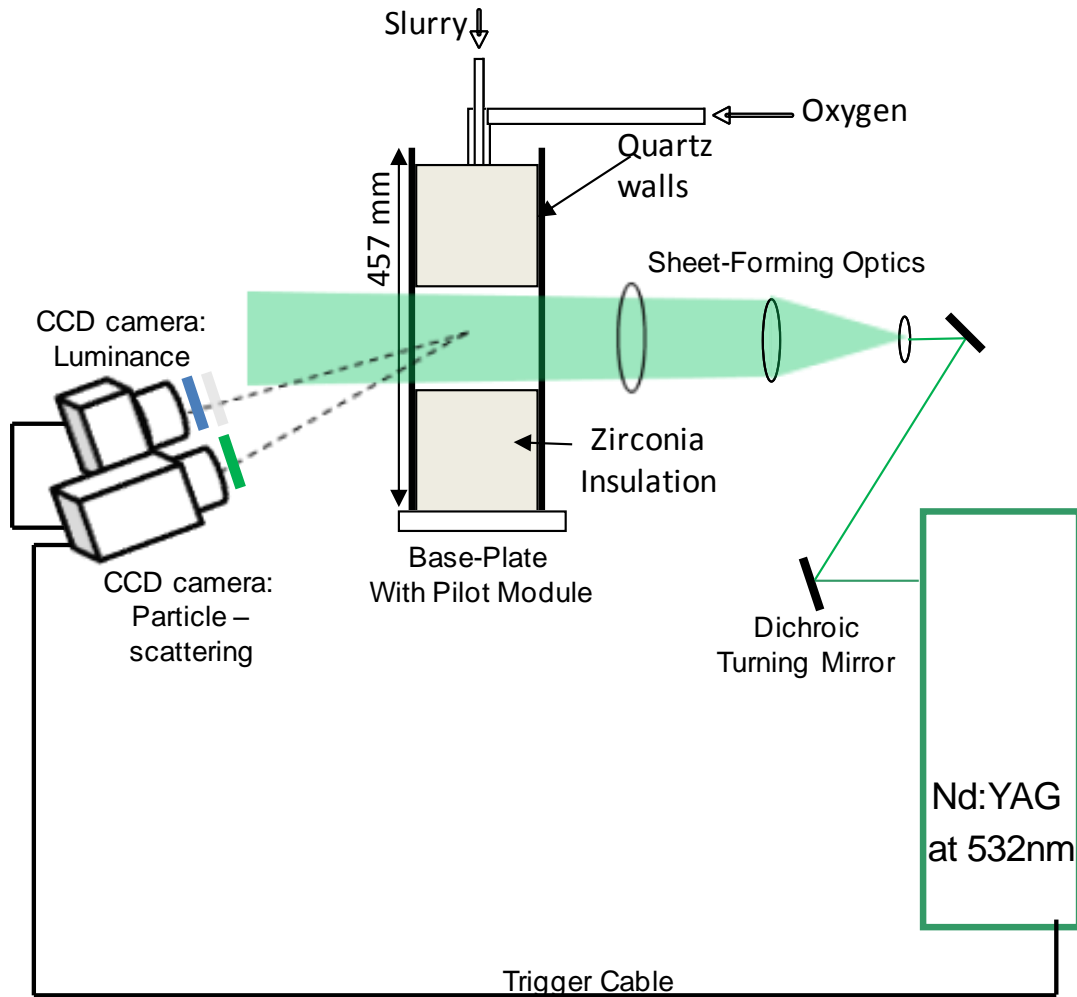
Figure 15. Optical layout of the particle-scattering and luminance-imaging setup

3.1.2.2 Spray Atomization Test Rig

The test rig consists of a spray chamber, illumination system and imaging system. The spray is back-illuminated by uniform diffuse light produced by an expanding Cu-vapor laser beam impinging on a translucent screen (shown in Figure 16(a)). Highly magnified shadow-images of the broken spray, similar to a representative image shown in Figure 16(b), produced downstream of the atomizer are captured using a CCD camera coupled with tele-converters. These images were processed using commercial a standard software package (ImageJ) to obtain statistics of the particle-size distribution. Presumably, these detected particles are isolated water-

droplets as well as solid-agglomerates with a surrounding water-layer. With sufficient illumination intensity, the transmitted light and consequently the signal-levels of the shadow-images of the water-droplets would be higher than that of the solid-agglomerates with a surrounding water-layer. One could thus classify these detected particles and thereby obtain varied statistics for each of the two groups. However, this was not possible in our current study.

The injector performance was studied corresponding to a baseline operating-condition characterized by mass flow-rates of 7.8 g/s for air and 7.5 g/s for slurry made out of a fine-powder batch with a Sauté Mean-Diameter (SMD) of 23 μm. Figure 17 provides the size distribution of the detected particles with a representative agglomerate-size (SMD) of 95.8 μm, obtained based on the statistics of the size-distribution of the detected particles. Notably, the atomizer performance can be may be significantly better when it is operated at higher mass flow-rate of air, say close to the baseline value of 10.2 g/s for the prototype combustor, as provided in Table 4.
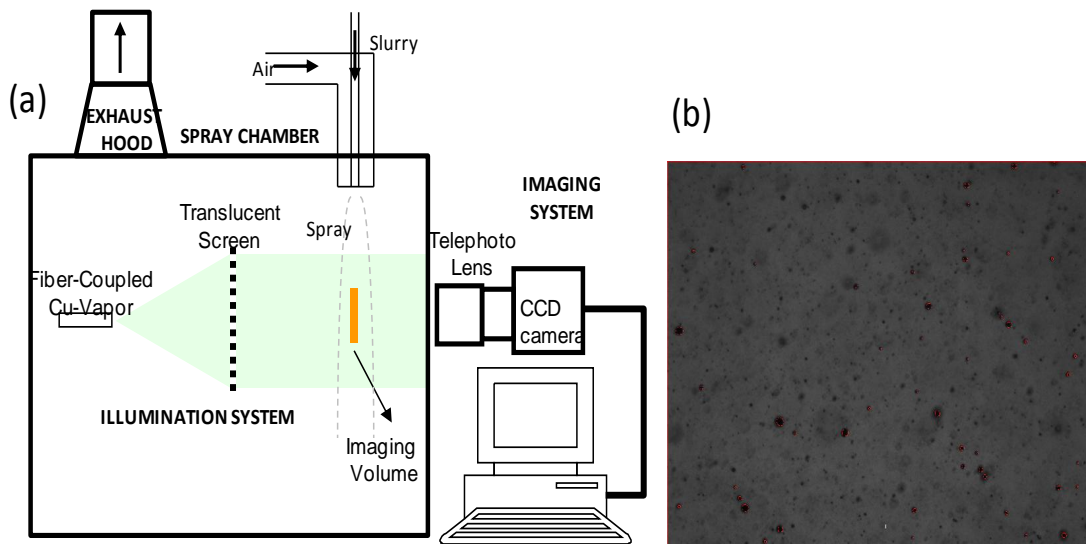
Figure 16. Spray atomization studies for injector performance evaluation: (a) optical layout of the test-rig and (b) acquired sample image with detected particles identified
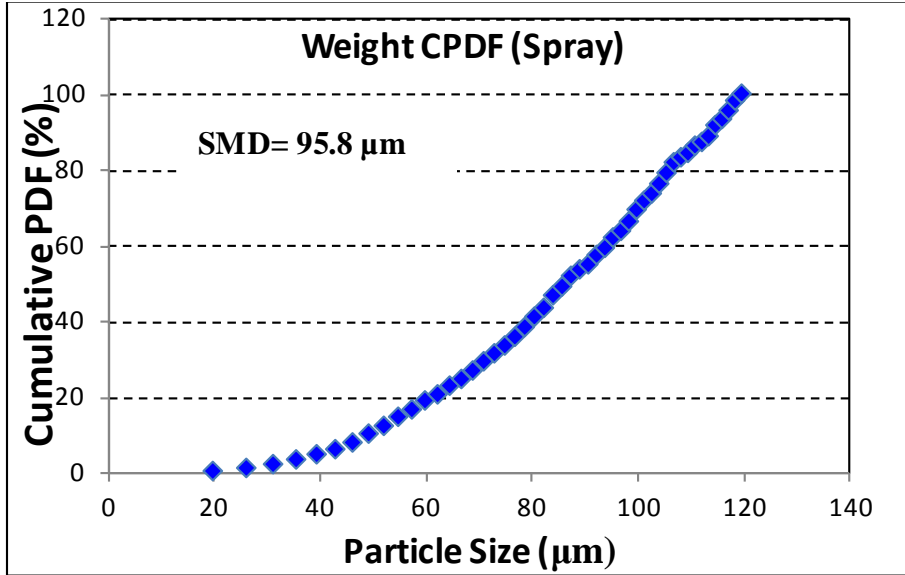
Figure 17. Size distribution of agglomerates produced by the co-annular atomizer during unconfined tests. The flow-rates of the fuel and oxidizer have been kept close to nominal loading conditions as possible.

3.1.3 Data Analysis and Interpretation Procedures

This sub-section describes the procedures adopted in the subsequent chapters of this thesis to analyze and interpret visualization images of the reacting flow-field. Specifically, a processing algorithm has been developed to convert the pixel-wise particle-scattering signal into a "local" fuel-conversion efficiency. Further, this sub-section also describes a processing technique based on the application of a threshold filter to raw particle-scattering images to determine various characteristics of the reactant-jet. This sub-section concludes with an investigation on the applicability of luminance imaging as heat-release markers to study the reaction zones of our solid-fueled SPRF combustor.

3.1.3.1 Local-Efficiency Map

As described in the previous chapter, for a petroleum-coke particle burning only at the exterior surface, the net burning rate can be approximated using a "shrinking–sphere" model. Consequently, the instantaneous radius can be related to the normalized extent of mass-loss or the fuel-conversion efficiency as:

$$\frac{r}{r_o} = 1 - \eta^{1/3} \qquad\qquad 3.2$$

Being proportional to the cube-root of the normalized extent of mass loss, the radius drops relatively slowly compared to the instantaneous mass of the particle during the quasi-steady phase of combustion. To cite an example, characteristic of the mean particle sizes of the relatively "fine" commercial grind powders, a 25 μm particle burning down to a 5 μm diameter corresponds to a 99% mass-loss for the particle. For these size-ranges, appropriate scaling laws can be used to relate the particle scattering-intensity (I) collected at a distance (D) to the instantaneous particle-radius (r) and the laser intensity (I_{laser}) as:

$$I = 4 I_{laser} \left(\frac{\pi r}{\lambda} \right)^2 \frac{F(n,\theta)}{D^2} \qquad\qquad 3.3$$

Here the directionality parameter ($F(n,\theta)$) may be taken approximately as constant since the signal-detection system is located farther away in comparison to the dimensions of the imaged location. Further, in actual experiments, the pixel-wise detected signal corresponds to scattering from particles (S_{Mie}) within the imaged probe volume overlaid on a background signal ($S_{background}$) resulting from elastic wall scattering and as well as radiation from the walls. Consequently, the above equation can be re-written as:

$$S_{Mie} = S_{background} + \sigma_{scattering} Q_E \Omega_{optics} I_{laser} N'' A_p \qquad\qquad 3.4$$

where $\sigma_{scattering}$ is the scattering cross-section, Q_E the quantum-efficiency of the detector, Ω_{optics} the characteristic collection – optics constant and I_{laser} is the laser intensity. Additionally, the total scattering area within the probe – volume is represented by the combined term $N'''A_p$.

As the measured shot-to-shot noise variation in the laser power is lesser than 2% of the average laser power for typical systems used in our study, it is possible to relate the normalized local particle-scattering signal (s) to the properties of the probe volume:

$$s = \left(\frac{S_{Mie,probe} - S_{background}}{S_{Mie,max} - S_{background}} \right) = \frac{N'''_{probe} A_{probe}}{N'''_{max} A_{p,max} \quad S\text{-}mie,max} \tag{3.5}$$

As described in the previous section, the slurry is sprayed into the co-flowing high-velocity oxygen jet. Further, temperature gradients can result in preferential transport of particles, a process commonly referred to as thermophoresis. Neglecting the secondary effects of non-uniformities in particle number-density arising from these aforementioned effects, the particle number density is inversely proportional to the local gas temperature. Consequently, the previous equation can be re-written as:

$$s = \left(\frac{Tg(\eta_{Mie,max})}{Tg(\eta)} \right) \left(\frac{A_p(\eta)}{A_p(\eta_{Mie,max})} \right) \tag{3.6}$$

Intuitively, the highest particle-scattering signal is obtained corresponding to the core of the unburned reactant-jet, which has the largest particles and the lowest temperature. Further, the local gas-temperature can be related to the local fuel-conversion efficiency, neglecting secondary effects of mixing or heat-losses. As a consequence, these equations can be combined to relate s to the local fuel-conversion efficiency (η):

$$s = \left(\frac{1-\eta^{2/3}}{T_o(1+\sum_{n=1}^{6} c_i \eta^n)} \right)$$

3.7

Here the co-efficients (c_i) are obtained by fitting a sixth-order polynomial curve through the gas temperature-efficiency curve shown in Figure 18. This technique has been employed to obtain a map of the local fuel-conversion efficiency from the corresponding particle-scattering image (see Figure 19).

c1	0.16
c2	8.9e-3
c3	-3.9 e-4
c4	6.2e-6
c5	-4.46e-8
c6	1.24 e-10
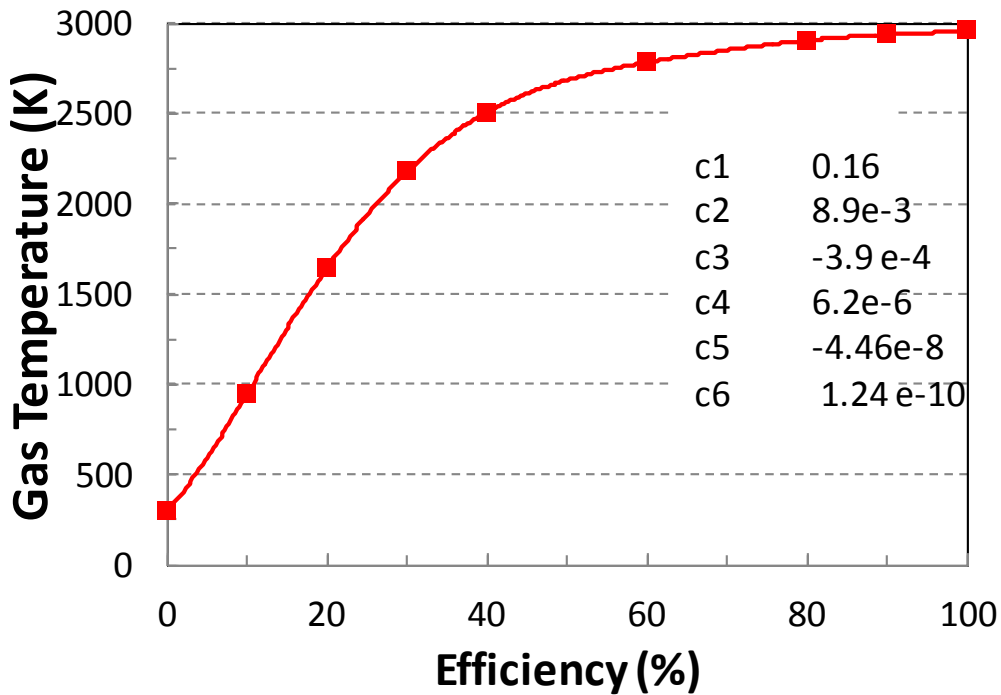
Figure 18. Variation of the calculated gas-temperature as a function of the local fuel-conversion efficiency (calculated curve-fit coefficients are tabulated adjacent to the plot)
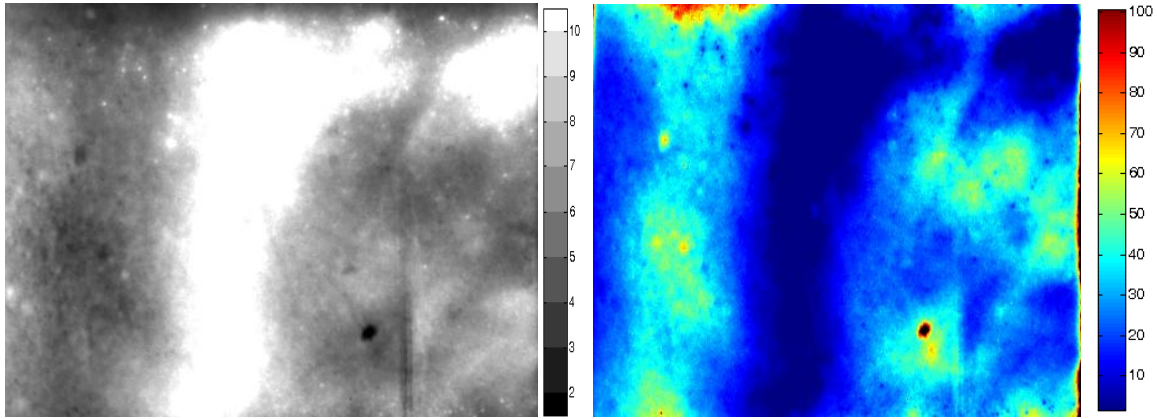
Figure 19. Raw particle-scattering image from the middle-imaged location of the prototype combustor (left) and the corresponding local-efficiency map obtained (right)

3.1.3.2 <u>Identification of Jet Centroid and Maximum Gradient</u>

Evidently, the sample particle-scattering image of the mid-combustor location shown in Figure 19 reveals the presence of an unburned reactant jet surrounded by burning products. To identify the spatial extent of the reactant jet in the image mentioned previously, a processing technique based on the application of a suitable threshold–filter on the scattering signal has been adopted. As a result, the gray–scale particle-scattering image in the previous figure is converted to a binary-image (Figure 20).

In a subsequent chapter of this thesis, the interfacial layer between the reactant jet and the burning products is examined to identify the main features. Consequently, it is important to identify a defining point within the jet as well as the intensity variation within the interfacial layer. The centroid of the binary image in Figure 20 is denominated as the center of the reactant jet while the maximum gradient direction is obtained by identification of direction along which the binary intensity value exhibits the maximum drop corresponding to a fixed distance. This is obtained as the direction along which the area enclosed by the binary intensity-distance curve is

48

a minimum. For example in Figure 20, the blue-cross represents the center of our reactant jet while the red line represents the maximum-gradient direction.
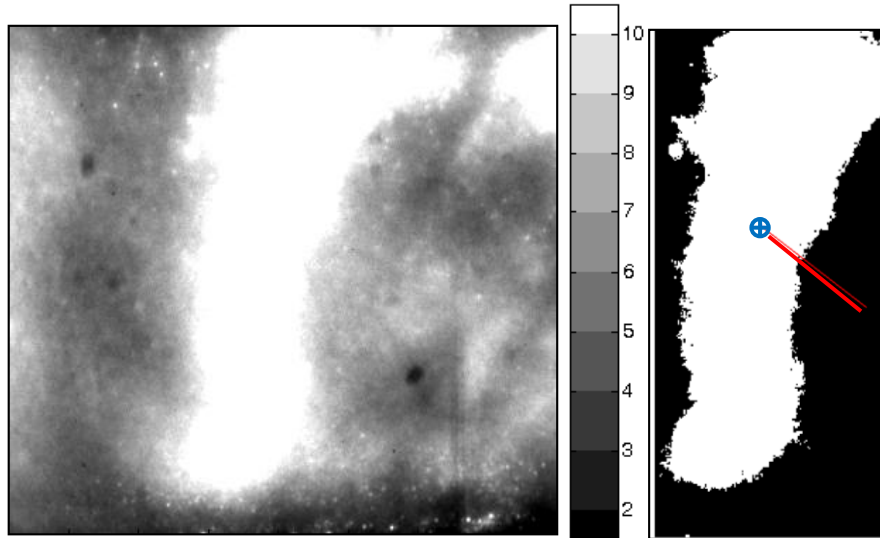
Figure 20. Raw particle-scattering image from the mid-combustor location (left) and the corresponding binary image obtained by application of suitable high-intensity threshold (right)

3.1.3.3 Interpretation of Luminance Signal

Direct imaging of short wavelength light emitted by the reaction-zones, i.e., corresponding to the radiation in the near-UV and visible region of the electromagnetic spectrum has been used extensively for studying the chemical processes in combustion systems. As this wavelengths range restricts the capture of radiative emission from radicals chemically formed in an excited electronic energy-state, this technique is popularly commonly known as chemiluminescence imaging. Chemiluminescence emission is generally considered to be a good indicator of heat release rate in hydrocarbon flames [35]. In our combustor burning pulverized solid-particles in a pure-oxygen environment, the particle temperatures typically reach the

adiabatic flame-temperatures, which are over 2500 K. Corresponding to these high temperatures, the blackbody emission intensity is very high.

As a consequence, isolation of a chemiluminescence signal from the blackbody radiation or the luminance signal may be challenging. In addition, the heterogeneous reactions associated with carbon conversion at the particle surface will not produce all the same chemiluminescence species associated with gaseous hydrocarbon fuel combustion. Thus, chemiluminescence imaging is not an attractive choice for the current conditions. For this reason, we focus on the luminance signal produced by the particle radiation.

Neglecting background radiation and viewing-angle changes within the imaged region, the luminance signal can be expressed explicitly in terms of optical properties of the band-pass filter as well as the local properties of the imaged region as:

$$S_{\text{luminance}} \approx \Omega_{\text{optics}} G(\lambda_{1,filter}, \lambda_{2,filter}, T_p) N^{'''} \varepsilon \sigma A_p T_p^4 \qquad 3.8$$

As described in the previous sub-section, the volumetric particle number-density may be related to the local gas-temperature (T_g), which is nearly equal to the particle-temperature for bigger larger particles in the range of a few tens of microns. Further, since a wide wavelength range (320-660 nm) is transmitted by the BG-18 filter employed here, the wavelength parameter in the above equation (G) can be assumed to be independent of the particle temperature. Consequently, the above equation may be re-written as:

$$S_{\text{luminance}} \approx K_{\text{luminance}} A_p T_p^3 \qquad 3.9$$

Presumably, the luminance signal will peak between the ignition-phase characterized by bigger, colder particles and the quasi-steady combustion phase characterized by smaller, hotter particles. As a consequence, it may be concluded that the luminance signal can is a reliable

marker of intense surface reactions and volumetric heat-release rates in combustion systems burning solid-fuels.

3.2   Modeling Methods

As outlined in Chapter 1, one of the three goals of this thesis involves the development of reduced order modeling of the transport and group-combustion processes in our combustor. Presumably, the transport of energy through product- entrainment and radiative transfer from the burning return-flow results in preheating of the incoming reactants and thus statically stable operation of the combustor. A simple reduced-order model can be used to examine the influence of entrainment; however, the product mixing conditions have to be prescribed. As described in Chapter 2, product entrainment levels of in the highly unsteady SPRF flow-field was have been quantified based on the statistics of directly measured using the Spontaneous Raman Scattering (SRS) technique for gas-fueled operation. As the Spontaneous Raman Scattering (SRS) signal would be overwhelmed by particle-scattering, similar measurements are not feasible in the current system.

Conceivably, a reduced-order idealized model based on the product fraction levels found in the previous SPRF geometry operating on gaseous fuel as well work as estimates for the current modeling. Therefore, a simple model that includes prescribed product mixing as well as an estimation of radiant fluxes in our combustor has been developed to examine the mass and energy transport effects on the incoming reactant jet, and it is presented in Sub-section 3.2.1. The predictions are used to support the results of visualization studies in understanding the mode of operation in Chapter 5, primarily as they pertain to the ignition behavior of the pet-coke particles in the SPRF.

Sub-section 3.2.2 describes the development of a second idealized model of group-combustion of particles. The eventual goal involves investigation of the effect of operating conditions on the surface-combustion rate and thus the fuel-conversion efficiency of the combustor. Similar to the idealized model developed for the estimation of transport processes, the group-combustion model uses appropriate assumptions regarding the residence time and the mixture properties that govern the group-combustion behavior of solid-fuels.

3.2.1 Particle Heat-up Model

As evidenced from the results of product-mixing studies on gas-fueled SPRF combustor presented in Chapter 2, the unique SPRF geometry allows for product-entrainment into the centrally injected reactant jet. This phenomenon occurs throughout the length of the incoming jet resulting in an axial variation of centerline product-fraction as well as the reactant-temperature. Further, the measured product-fraction and thus the reactant temperature were higher along the jet-edges than at the centerline of the combustor. Conceivably, in our prototype SPRF combustor operating on solid fuels, product entrainment results in the modification of the ambient gas-temperature and composition and thus the heat-transfer rates to the particle. Significantly, the particle-agglomerates in the incoming stream can also be heated directly by the radiation from the glowing return particles, in addition to the indirect route of entrainment.

The idealized one-dimensional model of particle-heating assumes that all the products are entrained at a particular axial –location, denoted by the term heat-feedback location (x_{hf}), as shown in Figure 21. Further, it is also assumed that the radiant intensity of the return-flow corresponds to the particle-temperature at the heat-feedback location. Based on these assumptions, it is possible to obtain a simplified model of the particle heat-up, as similar to that

developed by in reference [24]. The equations for is this 1-D equation model are described below.

$$M \frac{d}{dx} ZC_{p,p}(T_p) = F_{gp}(T_g(x, x_{hf}) - T_p) + aG(x, x_{hf})$$ 3.10

$$\Gamma_p = \left(\frac{3\lambda_g \rho_g Z}{r_p^2 \rho_p} \right) \left(\frac{-1}{8K_D r_p + 2K_{CH}} \right)$$ 3.11

$$G(x, x_{hf}) = \left(\frac{AT_p^4}{x^2} \right) \log \left(\frac{L + \sqrt{L + (r - rp)^2}}{L - \sqrt{L + (r - rp)^2}} \right)$$ 3.12

The first of the three equations provided above relates the rate of heating of the particle to the combined effects of conductive and radiative transfer, as a function of the distance along the centerline of the combustor. The heat-transfer coefficient of the conductive-term of this equation (F_{gp},) is obtained based on standard spherical heat-transfer analysis. The second RHS term represents the absorption of the axially-varying radiation field characterized by directionally-averaged intensity, $G(x)$ by the particle with an absorption-coefficient 'a'. The expression for the average intensity, $G(x)$ has been derived based on radiative heat-transfer analysis in cylindrical coordinate system.

Heat-Up
Reactor

G(x)
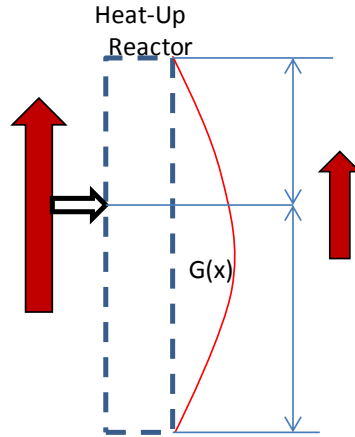
Figure 21. Schematic of the prototype combustor showing the incoming and return flow modeled as Heat-Up Reactor (blue-dashed) and Return-Flow PFR (red-dashed) respectively.

3.2.2 Group-Combustion Model

As detailed in Chapter 2, individual carbonaceous solid-particles burning in dust-clouds go through a short ignition-phase (Zone-I burning), which transitions to a relatively long quasi-steady combustion phase (Zone-III burning). The latter combustion phase governs the extent of fuel-conversion and consequently the performance of practical combustion systems like the SPRF combustor. This section develops an idealized statistically steady one-dimensional combustor model to predict the quasi-steady group-combustion of particles dispersed in gaseous oxidizer environment.

In the gas and liquid-fueled SPRF, the return flow was shown to consist of highly unsteady and spatially non-homogeneous burned products exiting the combustor. Presumably, when the fuel is slow-burning, like e.g. petroleum-coke, the relatively high velocity return flow would consist of particles burning in the quasi-steady or Zone-III combustion phase. As the

Stokes number calculated based on the measured mean agglomerate-sizes (97 μm) is lesser than unity, it may be assumed that the velocity lag between the gas and the particles are negligible.

Group-combustion of multiple particles in dust-cloud significantly depletes the local-oxygen concentration resulting in high heat-release rates and elevations in the ambient gas-temperature. Coupled conservation equations, as formulated by [24] have been appropriately modified to model the inter-particle effects and thus analyze the group-burning behavior in a characteristic Plug Flow Reactor (PFR). These are provided below:

$$M \frac{d(1-Z)}{dx} = \Gamma_p \tag{3.13}$$

$$M \frac{d}{dx}\left(Z C_{p,p}(T_p - T_o) + (1-Z)C_{p,g}(T_g - T_o) \right) = -\dot{Q}_{loss} + h_{het}\Gamma_p \tag{3.14}$$

$$M \frac{d}{dx} Z C_{p,p}(T_p - T_o) = F_{gc}(T_g(x) - T_p) - 4a\sigma T_p^4 + h_{het}\Gamma_p \tag{3.15}$$

For a given total mass flow-rate (M), these equations relate the axial variation of the gas-phase mass, total-energy of the dust-cloud mixture and the energy-balance for the particle-phase on the left-hand side to the corresponding source and the sink-terms on the right-hand side. The source term on the right-hand side of the first-equation represents the mass-production due to heterogeneous surface reactions.

Equation 3.14 and 3.15 are the total and particle-phase energy conservation equations respectively. As the Biot number calculated based on the measured mean agglomerate-size is significantly lesser than unity, it may be safely assumed that the temperature remains constant within the entire volume of the particle. As a consequence of the heterogeneous surface reactions, energy is released which appears as the corresponding source-term ($h_{het}\Gamma_p$) in these two equations. The sink term in Equation 3.14 represents the heat-loss per-unit length (Q_{loss}) through the combined effects of convective transfer from the gas-phase and radiative transfer.

The corresponding terms in Equation 3.15 is the radiative heat-loss term ($-4a\sigma T_p^4$). The additional term of the same equation represents the loss or gain of energy from the particle-phase to the gas-phase as a consequence of boundary-layer conduction. The heterogeneous combustion rates have been estimated using the following equations:

$$\Gamma_p = \left(\frac{3\rho_g Z}{r_p}\right)\left(\frac{-1}{8K_D r_p + 2K_{CH}}\right) \qquad 3.16$$

$$K_D = \frac{\rho_p}{3\rho_g D_{O_2}\chi_{O_2}\left(T_g/T_o\right)^{0.75}} \qquad 3.17$$

$$K_{CH} = \left(P_g\chi_{O_2}A\exp\left(\frac{-E_a}{RT_p}\right)\right)^{-1} \qquad 3.18$$

As the energy and mass source-terms have a strong dependence on the particle-temperature, these equations are numerically integrated using a "Stiff" ODE-Solver sub-routine (i.e. ODE15s routine of in MATLAB) to obtain the axial variation of properties of the PFR.

The predicted results, namely the PFR exit properties corresponding to a given residence time are dependent on those of the inlet, namely the species composition as well as the inlet-temperature. As described in the previous sub-section, entrainment and radiative transfer can significantly affect the gas-temperature and the composition. Further, these processes occur throughout the combustor and results in different properties at each location. Consequently, we have made simplifying assumptions about these effects. Essentially, the incoming temperature is held at a pre-determined value and the effect of entrainment on species-composition was examined using an adiabatic stirrer. This stirrer element mixes the products exiting the combustor and the reactants in the ratio f_p:1, as shown in Figure 22. Chapter 4 describes the methodology adopted involving the chosen values for the model parameters.
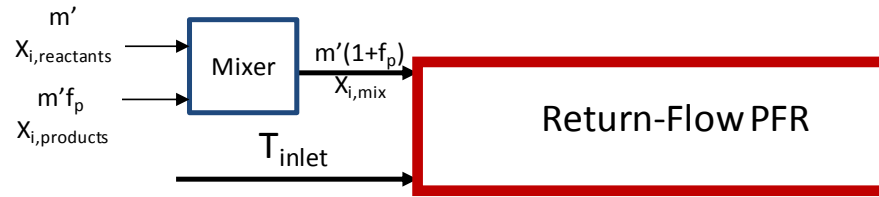
Figure 22. Reactor layout for the quasi – steady group combustion model of the prototype combustor showing the adiabatic mixer (blue – box) and the Plug Flow Reactor (red – box)

CHAPTER 4

PROTOTYPE COMBUSTOR PERFORMANCE

This chapter presents experimental results of the prototype combustor performance and compares them with the results of modeling methodology developed for design improvements and scale-up for practical applications. Section 4.1 describes the operation of the prototype combustor designed based on central injection SPRF geometry corresponding to baseline conditions. The experimental technique based on the use of exhaust sampling and analysis has been used to characterize static-stability and measure fuel-conversion efficiency corresponding to baseline and other operating conditions of interest.

In section 4.2 of this chapter, the idealized modeling methodology developed in Chapters 2 and 3 has been applied to predict the extent of burning. The predicted results are compared with the acquired data corresponding to the different conditions tested. Further, the idealized methodology is used to predict the performance of the combustor for eventual application involving steam-generation at high operating pressures. The validity of assumptions and the importance of predictions are discussed. Section 4.3 concludes with the main findings of the combustor performance and the model predictions as well as recommendations for better understanding of the reacting flow-field.

4.1   Prototype Combustor Tests

The prototype combustor was tested for static stability, initially, corresponding to a baseline condition of interest. The performance was gauged using the exhaust sampling and analysis technique outlined in the previous chapter. The same technique was used to investigate the effect of operating condition, namely the total mass-loading, particle-size and water-dilution

on the performance of the system. The results of the baseline and off – baseline tests are detailed below.

4.1.1 Baseline Operation

The baseline operating condition corresponds to a power of 125 kW-th. The fuel flow-rate is determined by the baseline operating power and the oxygen flow-rate was adjusted such that the fuel and oxidizer met at near stoichiometric proportions within our prototype combustor. The pilot-flame was used to heat and subsequently ignite the reactants, namely oxidizer and petroleum-coke slurry prepared using the procedure described in Chapter 3. The combustion process appeared to be visibly self-sustained, characterized by the presence of bright glowing particles exiting the burnout-section (Figure 23). The composition of exhaust-gases were continuously monitored and recorded during the duration of the test.

Figure 24 shows the variation of the measured exhaust-gas composition as a function of time during the testing period. Presumably, the CO_2 mole-fraction decreased and O_2 increased following the introduction of the slurry (t=660 s) because of the quenching effect of the water in the slurry lines. After the pilot-air and pilot-fuel were turned off, i.e. at t=738 s, the measured CO_2 mole-fractions increased whereas the corresponding O_2 values decreased. Steady-state was reached at around t=978 s, characterized by statistically unvarying mean and peak-fluctuations of lesser than 2%. The readings corresponding to this nominal steady-state point were used for the calculation of fuel-conversion efficiency based on the procedure described in Chapter 3. The measured CO value of 150 ppm at the nominal steady-state point represents a negligible fraction of the carbon-conversion, even after accounting for the effects of dilution in the sampling system.

The procedure discussed in Chapter 3 was used to calculate the temporal variation of fuel-conversion efficiency during the transition-period between turning off the pilot (t=738 s) and the nominal steady-state point (t=978 s) (Figure 25). Notably, the measured fuel-conversion increased from 27% to 64% during the transition period and stayed nearly constant thereafter, proving that the combustion process was self-sustained.
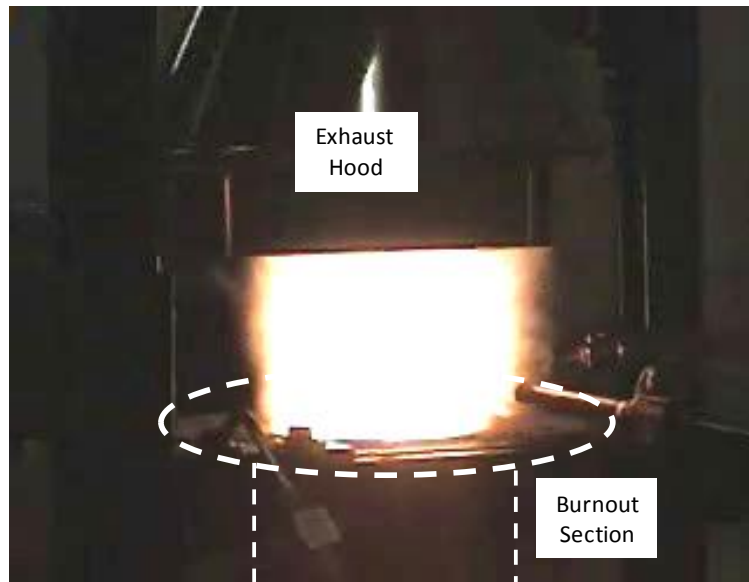
Figure 23. Photograph of the prototype combustor operating without pilot fuel at the baseline operating conditions with a bright flame extending from the combustor exit.
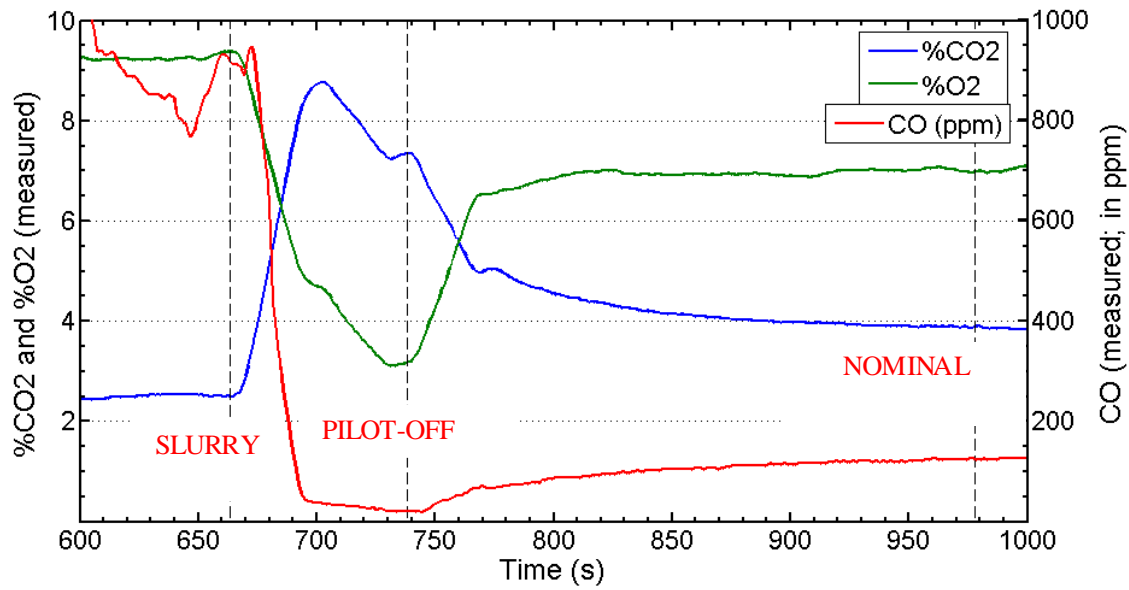
Figure 24. Temporal variation of the mole-fractions of species in exhaust gases measured by the ESA system
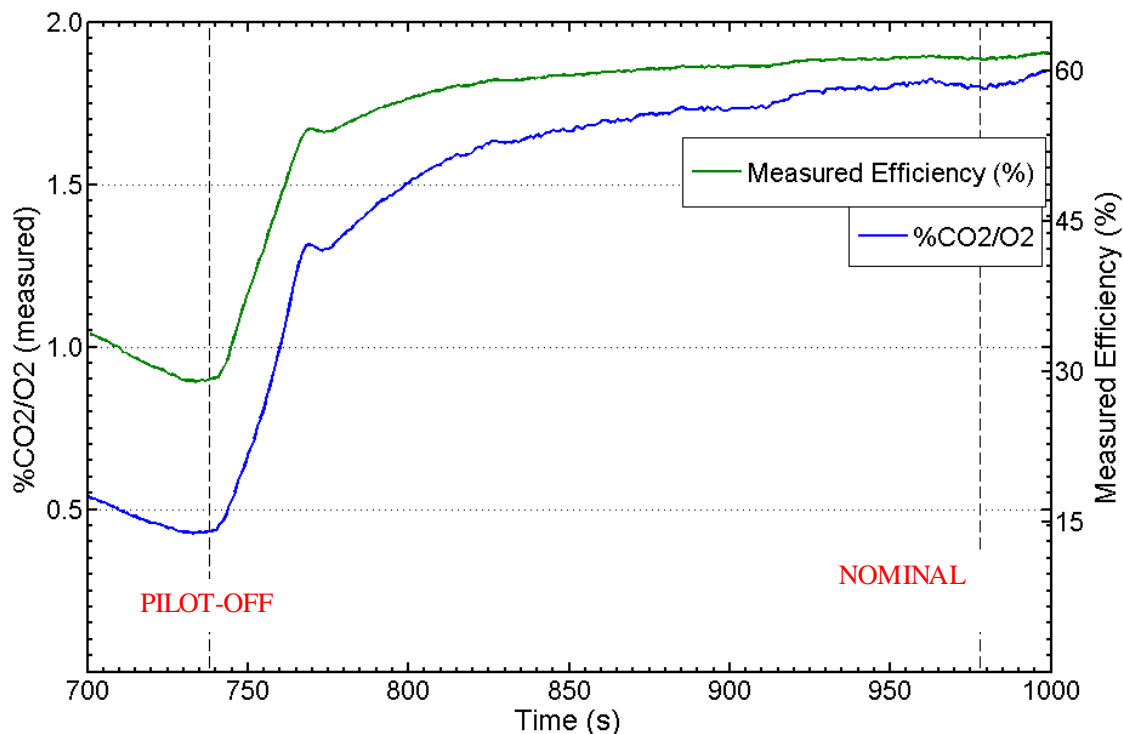
Figure 25. Temporal variation of fuel-conversion efficiency determined from the measured CO_2/O_2 mole-fraction ratio

During the transition-period, the temperature of the water flowing out of the cooling jacket was monitored. Further, steady-flow analysis was used to estimate the extent of the absolute and relative heat-loss rates, normalized by the thermal-power of the system. Presumably, the higher thermal inertial of the system is responsible for the relatively longer duration taken by the outlet water-temperature and thus the heat-loss rates (Figure 26) to reach their steady-state values. Further, it is also evident from the same figure that the heat-loss rate represents approximately 51% of the thermal power of the system, corresponding to the nominal steady-state point. Presumably, lower product temperatures resulting from these heat-loss rates are responsible for slower surface kinetic-rates resulting in longer burn-times.
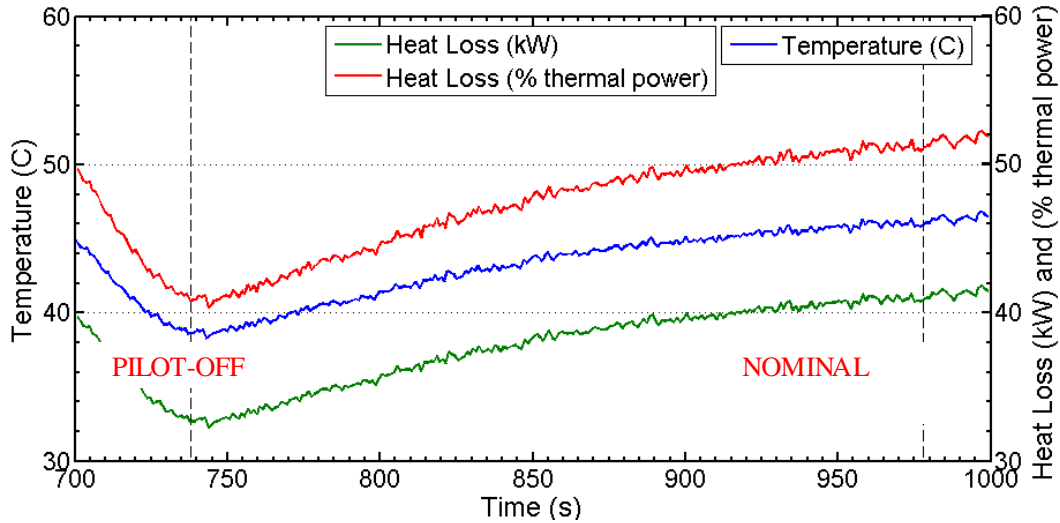
Figure 26. Temporal variation of outlet water-temperature and the heat loss-rate during the transition period

4.1.2   Effect of Operating Conditions

The static stability of combustion process was investigated at other operating conditions of interest, namely the total mass-loading, slurry-water content and the mean particle-size. Self-sustained operation was possible corresponding to the initial round of tests involving variation of the total mass-loading of the system, holding the latter two parameters constant. Evidently, the fuel-conversion efficiency decreased by close to 6.0% and the normalized heat-loss stayed nearly invariant and close to 50% of the thermal power output of the system when the total mass-loading was raised from the baseline-condition to the highest loading-case (Figure 27). As discussed in Chapter 2, the relatively-slow, quasi-steady Zone-II burning of petroleum-coke chars is governed by Arrhenius surface surface-kinetics rates which are strongly dependent on particle-temperatures. Presumably, incomplete combustion is the direct consequence of both insufficient residence time as well as heat-losses resulting in lower particle-temperatures and associated surface kinetic-rates.

63

Next, the effect of particle-size was investigated in three separate tests using three different powder batches, denominated as: (a) "fine" powder-batch ($D_{p,avg}$=23 μm), (b) "medium" powder-batch ($D_{p,avg}$=42 μm) and (c) "coarse" powder-batch ($D_{p,avg}$=90 μm) , at the mass flow-rates corresponding to the baseline operating condition. Similarly, the effect of reactant dilution was investigated by varying the water-content in the slurry from 50.0% corresponding to the baseline operating condition to around 65.0% in four different stages within the same test. The prototype combustor experienced a loss of static stability characterized by a sudden-drop in measured CO_2/O_2 ratio when it was run without pilot-flame on the coarse powder-batch. Similar behavior was observed when the water content in the slurry was raised from 60.0% to 65.0%. However, the exact position of blowout limits in the size range of 42 to 90 μm as well as dilution levels between 60 and 65% requires to be determined (Figure 28).

Bigger particles, in general, are characterized by lower net surface combustion rates and consequently volumetric heat-release rates. This affects the net heat-feedback and thus the static-stability of the combustion process corresponding to the coarse powder-batch. Similarly, it may be postulated that the quenching effect of the added water results in loss of static-stability corresponding to change in water-content from 60.0% to 65.0%.

The prototype combustor was found to be statically stable corresponding to baseline and higher mass-loadings. Further, the static-stability was unaffected for mean particle-sizes of up to 42 μm and water-content of 60.0% in the slurry. For these operating conditions of interest, the variation in the fuel-conversion efficiency was found to be lesser than 6.0% of that corresponding to the baseline operating condition. As a consequence, it may be concluded that the prototype combustor represents a relatively robust system whose performance is not significantly altered by a range of variations in operating conditions.

The "robustness" of flame-holding of the SPRF operation on pet-coke slurry is ascertained by comparison with the results of previous studies reported in Chapter 1[16] . The authors reported that the combustion process was statically unstable without support fuel and preheating of incoming air enriched with oxygen. Further, these tests do not explicitly report the fuel-conversion efficiency of petroleum-coke tests, although they allude to the low carbon content in the residual ash for these tests. In comparison, our studies show that the SPRF combustor is a robust flame holding geometry for pet-coke combustion, without support fuel or external preheating. Although our tests use pure oxygen, as opposed to enriched oxygen, the power density is significantly higher (MW as opposed to kW). Significantly, the combustion process was statically stably for slurry water content as high as 60.0%, as opposed to the 30.0% corresponding to the tests mentioned earlier.

The possibility of improvements in the design, especially for future applications is dependent upon investigation of practical factors like heat-losses and operating pressure, which are likely to affect the net surface kinetic rates and consequently the extent of fuel conversion to products. The following section analyzes the performance under these conditions using the idealized model developed in Chapter 2. The agreement between the data and predicted results is also discussed.
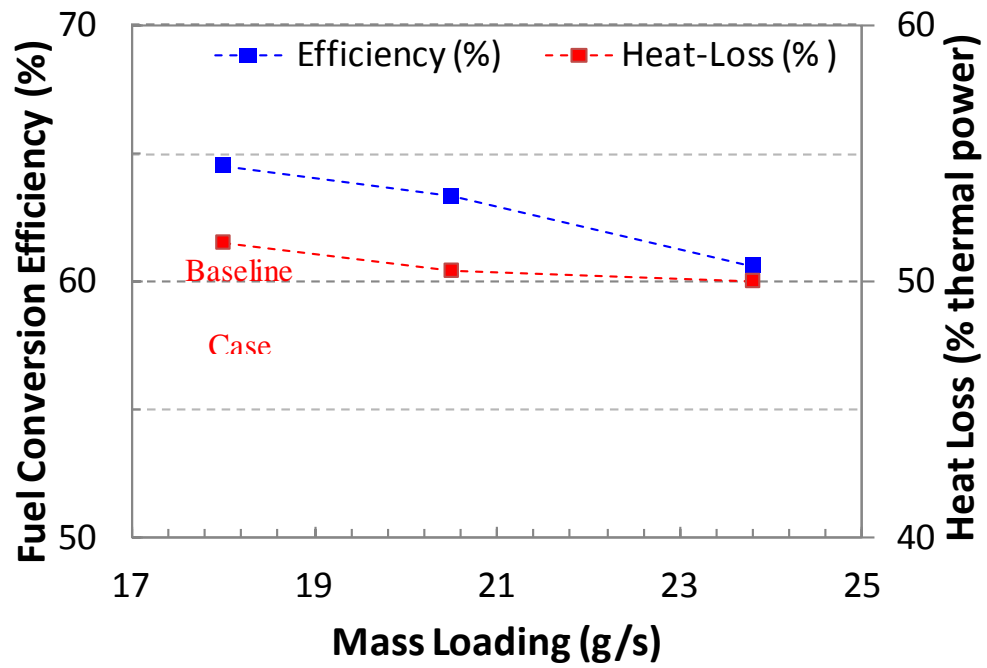
Figure 27. Variation of fuel-conversion efficiency and normalized heat-loss rates as a function of mass-loading
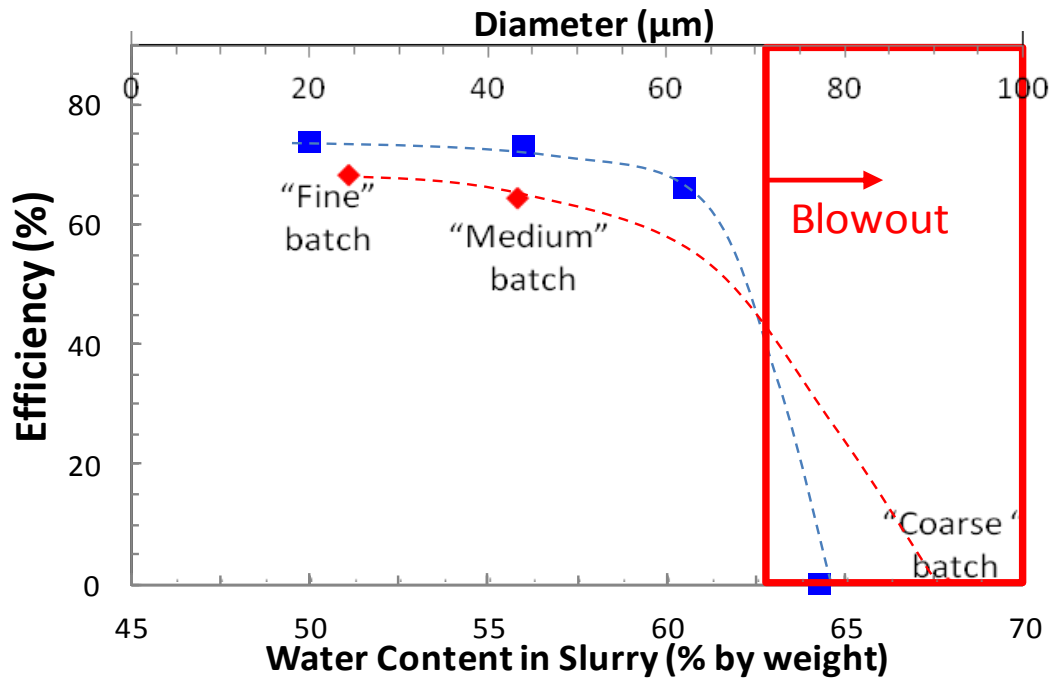
Figure 28. Dependence of static-stability of the prototype combustor on operating conditions: slurry water-content (blue – squares) and particle – size (red – squares)

4.2 Modeling

This section deals with the performance evaluation of the numerical model developed in Chapter 3 for group combustion of particles. As described, the model makes some implicit assumptions regarding the mode of operation. The primary assumption is that the particles have been preheated to a sufficiently high temperature before the quasi-steady combustion phase. Further, it also assumes that the mixture composition has been modified based on product entrainment and that the spray is characterized by a mean agglomerate size. Sub-section 4.2.1 describes the methodology adopted for the choice of model as well as the input parameters. This section also compares the predicted results with the measured values corresponding to different operating conditions.

4.2.1 Model Implementation

As described in Chapter 3, the main model parameters are the input properties as well as the main model parameters are the input properties as well as the Plug Flow Reactor (PFR) residence time. We first shift our focus on the estimation of the input properties. The reactant inputs comprise of the mass flow-rates, mixture-composition, mean agglomerate-sizes and the reactant temperature. The reactant mass flow-rates for the model correspond to those of the baseline and other off-baseline conditions characterized by higher mass-loadings. In comparison, estimates are obtained for the mean agglomerate-sizes as well as the reactant-temperature. The statistics of agglomerate size distribution measured in un-confined injector tests has been used to calculate a representative Sauter Mean Diameter (SMD) of 97 μm, taken as the mean agglomerate-size for the model. Further, since the reactants are injected through an insulated injector without preheating, the reactant-temperature is estimated to be close to the room-temperature value of 300 K.

Next we shift our focus on the estimation of the intrinsic model parameters, namely the residence time in the combustor as well as the heat-loss parameter. As described in Chapter 3, the residence time for a given flow-rate of the incoming flow is directly related to the volume of the Plug Flow Reactor (PFR) model. Based on the results of luminance imaging presented in the following chapter, the majority of heat-release occurs in the mid-combustor location and the burning packets turn around and exit on either side of the central injector. As a consequence, the net PFR volume is taken as the total combustor volume less the volume of the near-stagnation location, which roughly accounts for one-third of the total volume.

In comparison, the heat-loss parameter is estimated based on the measured values of the heat-loss rates from the combustor based on the steady-flow analysis performed on the cooling

water. As presented in the Section 4,1, the measured heat-loss was approximately 50% of the total thermal power output of the system and was found to be invariant with changes in total power output of the system. To account for this, the heat-loss parameter defined below is held constant corresponding to the different cases simulated:

$$Q' = \frac{\dot{W}_{loss}}{\Delta H \, \dot{m}_{fuel}}$$

4.1

4.2.1.1 Parameter Errors and Sensitivity Prediction

There are uncertainties in the approximated values for the various model parameters. To cite an example, errors in predicted results may exist because of the choice of approximation of distribution of the product fraction levels and the agglomerate-sizes by the mean values. Similarly, other sources of error include estimation of the incoming temperature and the net combustor volume. This sub-section examines the sensitivity of the predicted results to the errors in the various parameters of choice.

While most of the parameters have been obtained based on measured values, a few of them like the product-fraction level (f_p) and the reactant-temperature have been assigned nominal values based on previous SPRF studies. Consequently, the errors in these parameters have also been assigned nominal values, as provided in Table 5. In comparison, the PFR volume has been estimated based on the results of visualization studies presented in the following chapter. Based on this, it was found that the near-stagnation location was devoid of significant heat release rates. Presumably, as data is non-existent between the mid-combustor and the near-stagnation locations imaged, the combustor volume corresponding to this location is a good estimate of the errors associated with estimation of the PFR volume. Similarly, as good estimates of errors for the heat-

loss parameter as well as the reactant temperature do not exist, they have been assigned nominal

values of 10%.

Table 5. Reactant and model parameters chosen for the idealized model

Model Parameter	Nominal Value	Error	Error (%)
Heat Loss Parameter (Q')	0.937	-	±10 (Nominal)
D_p (μm)	97	±10	±10
$V_{PFR}/V_{combustor}$	0.67	±0.14	+30.0%
Product Fraction (f_p)	0.8	±0.2	+5.0%
Reactant Temperature (K)	1450	-	±10 (Nominal)

Next we examined the sensitivity of the predicted result (Σ_i), as defined below, to the

errors in each of the various parameters (P_i) chosen:

$$\Sigma_i = \frac{\partial(\log \eta_{predicted})}{\partial(\log P_i)}$$

4.2

The predicted results are most sensitive to the normalized PFR volume and the mean

agglomerate sizes, as compared to the other parameters. Smaller particles and lower product

fraction result in higher fuel-conversion efficiency resulting in negative sensitivity coefficient.

Using the errors in individual parameter as well as the sensitivity of the predicted results to the

corresponding errors, it has been possible to the obtain limits on errors in the predicted results.

The following sub-section compares the baseline predicted results as well as the errors obtained

based on the predicted results with the measured values.

70

4.2.1.2 Model Predictions

Figure 29 shows the predicted results as a function of the normalized mass-loading as well as the measured values corresponding to these conditions. The data agrees with the predicted results within the limits of the errors tabulated above. As a consequence, the model can be used to predict the effect of operating conditions on the performance of the system.

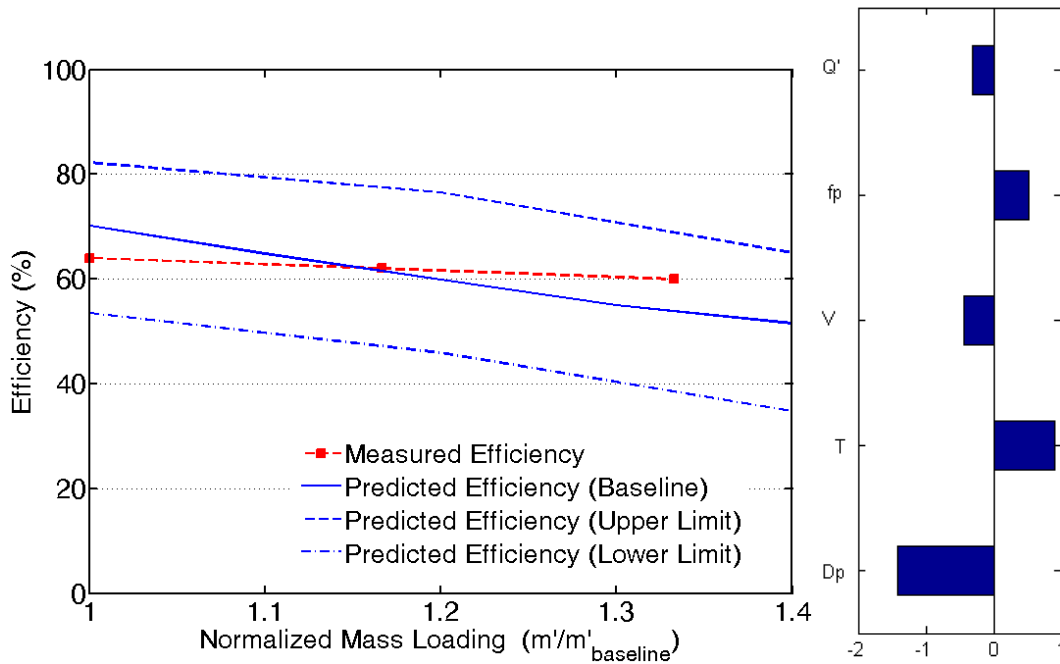**Figure 29. Comparison between the measured and the predicted fuel-conversion efficiencies corresponding to different loadings under conditions of nominal parameters (solid blue – line) and errors in nominal parameters (broken blue – line)**

The following section examines the effect of design changes on the performance of the prototype combustor based on the predictions of the modeling methodology developed previously.

4.3   Future Design Considerations

As the measured fuel-conversion efficiency suggests incomplete combustion of fuel, design modifications needs to be incorporated in order to attain complete combustion of fuel. As evident from the results of sensitivity analysis in Figure 29, the fuel conversion efficiency is enhanced by smaller agglomerates, higher residence time as well as lower heat-losses. Higher values for injection velocity and combustor volume adversely affect the injector pressure drop and the power density further and thus the practicality of the combustor design. Another practical concept involves operation at high-pressure conditions, typical for applications that require high power densities and high-pressure flue-gases, as described in Chapter 1. Based on the modeling scheme developed in Chapter 3, it is also evident that higher operating pressures enhance the surface reaction rates, thereby raising the overall fuel-conversion efficiency.

The performance of the prototype combustor at higher operating pressures was examined based on predictions of the modeling scheme, holding all other parameters constant with the exception of the operating pressure. As evidenced by the results shown in Figure 30, fuel-conversion efficiency increases and asymptotically reaches complete combustion corresponding to an operating pressure (P_{cc}) of around 1.5 atm. For a similar injection velocity as the baseline operation case, the injector pressure drop rises sharply with the operating pressure. In order to limit the injector pressure drop, it is necessary to lower the injection velocity resulting in bigger mean agglomerates. As evidenced by the results in the same figure, the asymptotic pressure limits (P_{cc}) increases with the mean agglomerate sizes, reaching typical values of 6.0 atm for mean agglomerate sizes thrice the size of the baseline value. Presumably, the prototype combustor is suitable for high-pressure applications as the high-limit value (P_{cc}) is lower than the characteristic operating pressures for such applications.
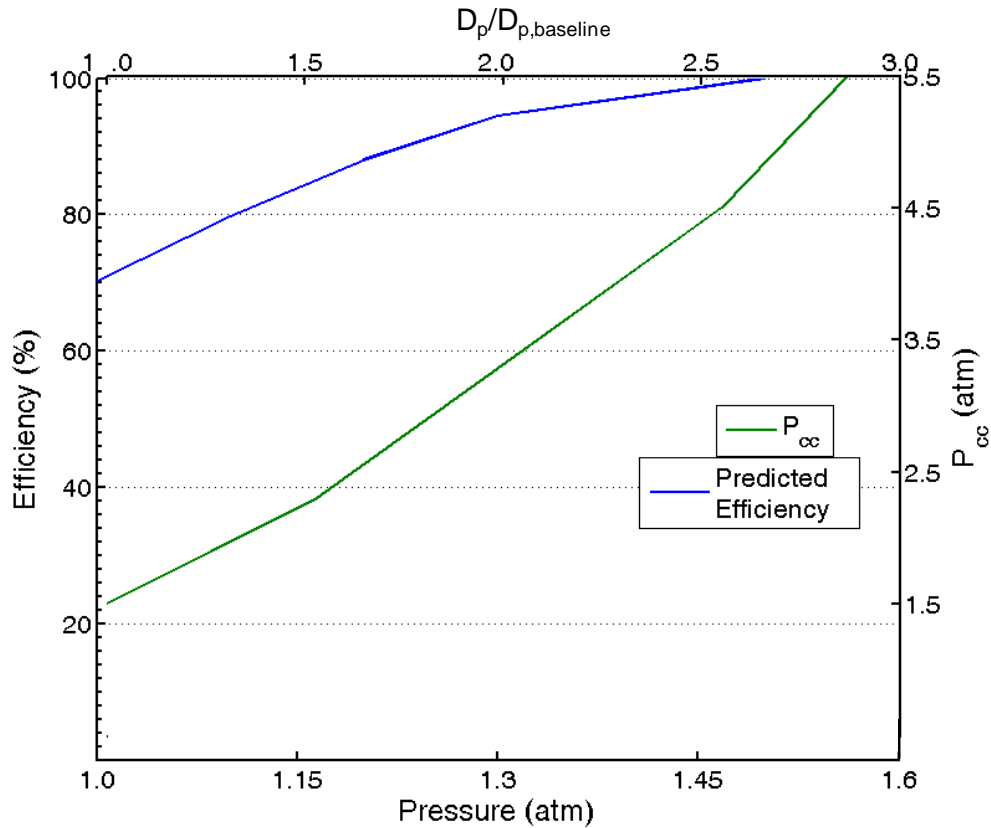
Figure 30. Variation of the predicted Fuel Conversion Efficiency of the prototype combustor as a function of the operating pressure (blue) and the combustor pressure required for complete combustion of the fuel (green) as a function of the mean agglomerate size

4.4   Concluding Remarks

This chapter examined the performance of the prototype-combustor corresponding to a baseline operating condition, preset by unique design requirement. The exhaust sampling and analysis system established static-stability corresponding to this baseline operation based on statistically unvarying measurements corresponding to a nominal steady-state condition. Further, statically stable operation was confirmed using the exhaust-sampling technique corresponding to different operating conditions involving variation of total loading, mean particle-size and the

water-content of the slurry. In comparison with a conventional quarl-geomtery, SPRF operation on pet-coke slurry has been shown to be more robust, as self-sustained operation has been possible corresponding to a range of conditions. The measured fuel-conversion efficiency confirmed incomplete fuel-combustion, postulated to be the combined result of residence time as well as heat-losses.

The performance was analyzed using a mathematical model developed based on some assumptions about the mode of operation. Specifically, internal exhaust gas-recirculation was assumed as the dominant heat-feedback mechanism for the ignition and quasi-steady burning of the agglomerates. The product-recirculation levels were obtained based on the product mixing studies on the gas-fueled SPRF combustor operating in the non-premixed mode. The predicted results appear to corroborate the effect of residence time and heat-losses on incomplete combustion of fuel. Design practicality dictates complete fuel-combustion as well as operation under high-pressure conditions. The predictions of the idealized model suggests that surface kinetic rates and consequently fuel-conversion efficiency is enhanced by higher operating pressures. Overall, the prototype combustor, with the inclusion of engineering modifications to minimize heat-losses, appears to be a promising concept for Direct Steam-Generation (DSG) applications.

As mentioned earlier, the model was developed based on some assumptions about the mode of operation as well as the reacting flow-field of the prototype combustor. The validity of these assumptions requires confirmation based on an analytical treatment of the relative dominance of the various other heat-transfer modes like radiation and conduction as well as visualization studies of the reacting flow-field. These results are presented in the following chapter.

CHAPTER 5

SOLID FUELED OPERATION

The previous chapter compared the results of the prototype combustor performance and the predictions of the idealized numerical model for quasi-steady burning of particles, corresponding to various operating conditions. The experimental results were within the predicted range of numerical results, accounting for the corresponding range of model parameters and their respective sensitivity to the predicted results. Various assumptions were employed in the development of the idealized model regarding the nature of the reacting flow-field and the primary mechanisms of operation. These assumptions need to be investigated; this is the primary goal of this chapter.

The first section presents the results of visualization studies performed on an optically accessible combustor, similar in geometry to the prototype combustor tested in Chapter 4. Specifically, Section 5.1 examines the extent of fuel-dispersion, heat-release locations and the various physical processes that control the behavior of the reactant jet. Section 5.2 details the results of various image processing and numerical analysis schemes undertaken to support the theories formulated previously. Section 5.3 provides a summary of the main findings.

5.1   Flow-Field Visualization

Visualization studies have been conducted on a modified version of the prototype combustor, equipped with optical access. As described in Chapter 3, the various combustor locations imaged are: (a) near-injector, (b) mid-combustor and (c) near-stagnation (end-wall). In this section, the results of analysis on mean as well as instantaneous particle-scattering images are presented with specific emphasis on the average fuel-dispersion within the combustor and the

75

various flow-features exhibited by the reactant jet. A similar analysis is applied to luminance images acquired simultaneous with the particle-scattering images to identify the combustor locations characterized by high surface (fuel oxidation) reaction rates.

5.1.1 Particle-scattering Images

Figure 31 shows the mean particle-scattering images at the three window locations in the combustor, with a brighter intensity indicating a higher scattering signal. The spacing between the images is not accurately represented in this illustration; the separation between locations is greater than indicated by their placement in the figure. Each mean image represents the average over nearly one hundred and fifty individual snapshots. Also included on the images are blue curves indicating the edge of the mean jet, determined with a threshold algorithm. The axial variation of the normalized width (W/D) of the incoming jet obtained from the edges is shown in the right side of the figure. As evidenced from these results, the incoming jet, on average, becomes slowly wider in the near-injector location (X/D<7), grows substantially in width by the beginning of the mid-combustor location, then narrows around X/D=15. Presumably, the incoming-jet breaks up and mixes substantially so that there is no longer a large region of cold reactants farther downstream (at least not on average). Further, the mean scattering from the imaged region near the bottom of the combustor indicates absence of significant amount of cold reactant jet penetration.

Next we analyze the instantaneous particle-scattering images to study the dynamics of the incoming jet corresponding to the different imaged locations. For the images in Figure 32, the incoming jet is identified using regions characterized by higher scattering signal, in comparison with the burning products. Clearly, the incoming reactants in the near-injector location are confined to the centerline of the combustor, and also display characteristic features of

76

atomization and mixing to form reactant packets. Similarly, the incoming jet in the mid-combustor location is also associated with breakup into reactant packets, although with a higher degree of lateral movement. Presumably, these packets ignite and burn at this location as they are characterized by spatial variations in particle-scattering signal. These features of the incoming and return-flow are further examined based on analysis of the cross-section plots of the particle-scattering signal corresponding to these two different locations (Figure 33).

As evidenced from the results in Figure 33, the incoming flow, say $-0.5<Y/D<0.5$, is characterized by higher spatial gradients in the scattering signal in the near-injector location, as compared to the mid-combustor location. Evidently, there is higher degree of dispersion of the fuel in the co-flowing oxygen jet corresponding to the mid-combustor location than the near-injector location. Further, the return flow region, say $-2.5<Y/D<-1.0$ in the near injector location or $2.0<Y/D<4.0$ in the mid-combustor location, is also characterized by similar spatial variations in the particle-scattering signal. Presumably, this is because the products are at different stages of burning as they reverse direction and leave the combustor. The following sub-section quantifies the extent of local-fuel conversion.
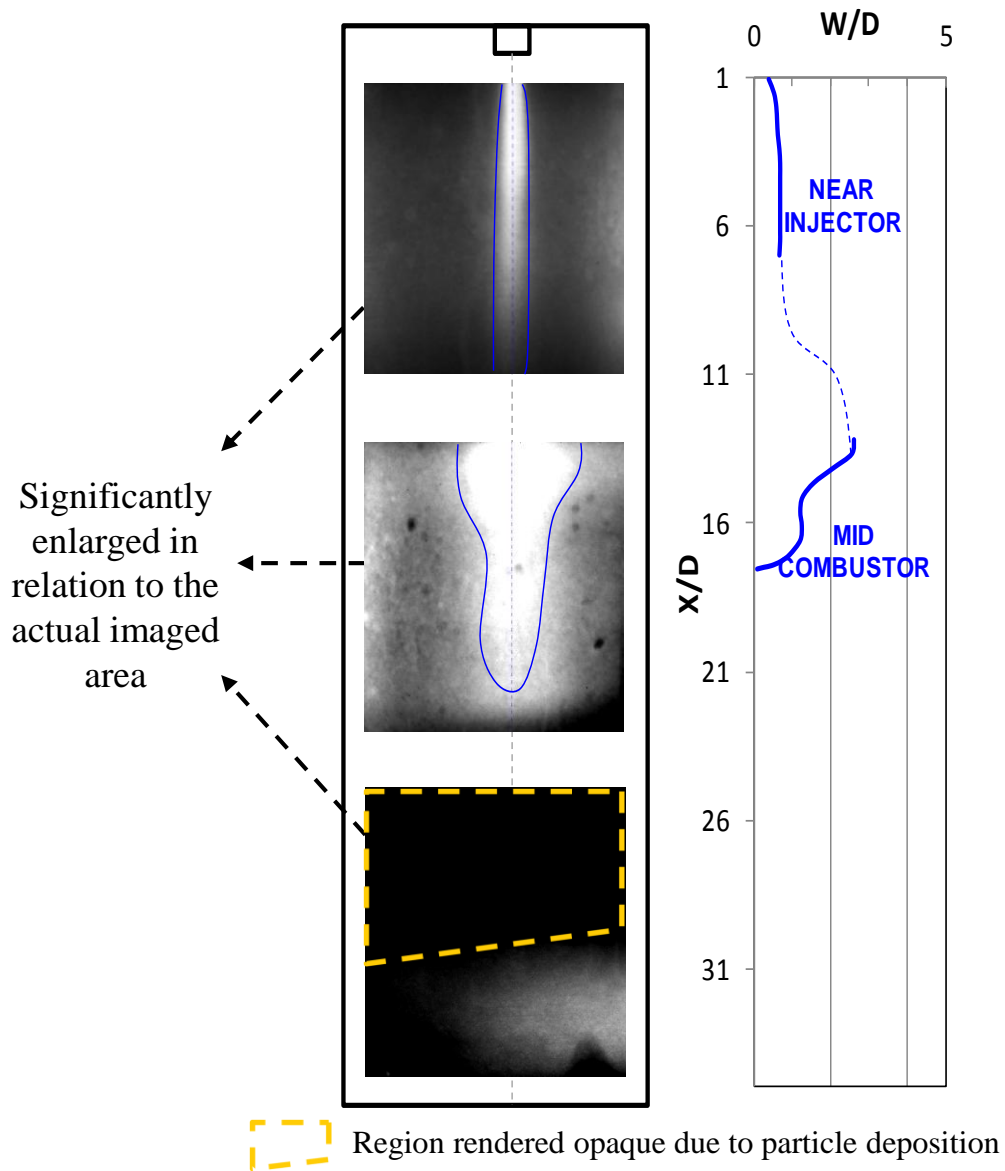
Figure 31. Mean particle-scattering images from the three different imaged locations of the combustor (left) and the normalized jet-width as a function of the normalized axial distance (right)
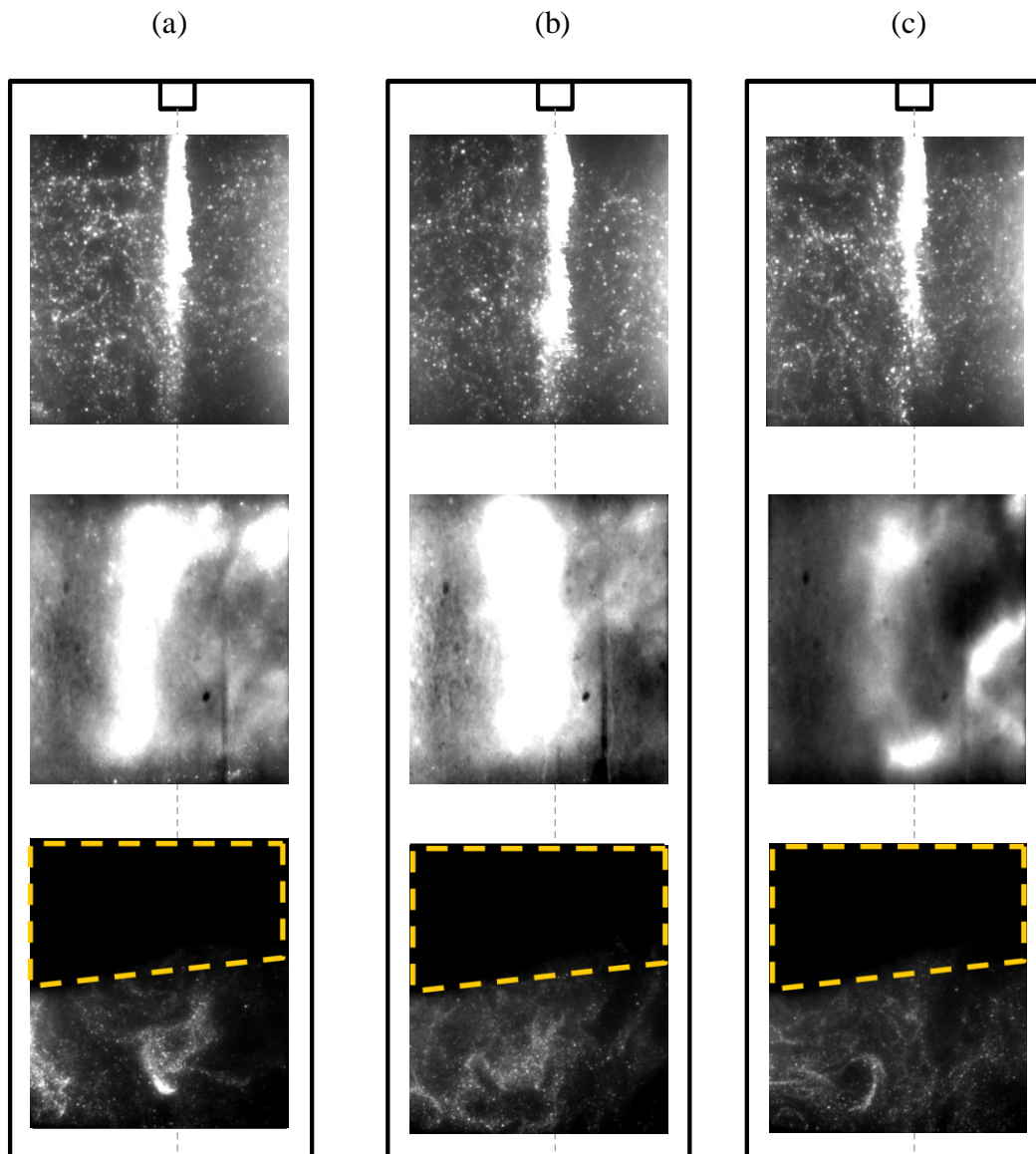
1) 〔- - - 〕 Region rendered opaque due to particle deposition
2) Image sets (a), (b) and (c) – significantly enlarged in relation to the imaged area

Figure 32. Instantaneous particle-scattering images from the three different imaged locations of the combustor
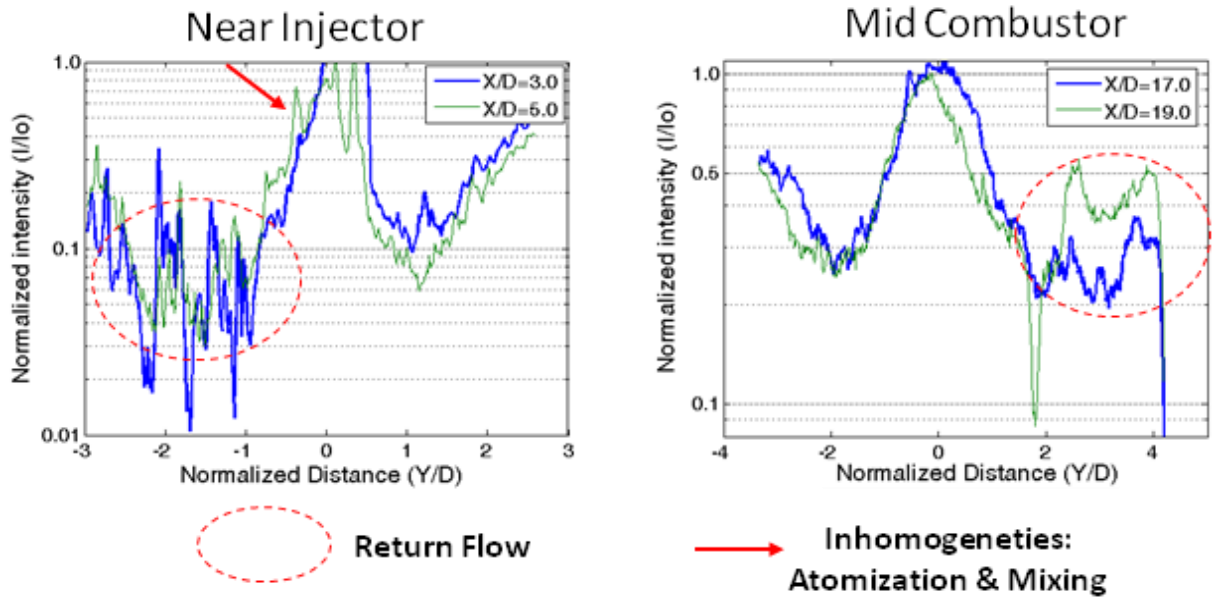
Figure 33. Cross-sectional variation of instantaneous particle-scattering signal across the width of the combustor for different axial locations of the corresponding: near-injector (left) and the mid-combustor (right) images of Figure 32 (a)

5.1.1.1 Efficiency Map

The particle scattering images can be converted to fuel-conversion efficiency maps, based on the image processing technique described in Chapter 3. Typical instantaneous results are shown in Figure 34, with the false color map indicating the level of conversion of the pet-coke fuel, e.g., 0 indicates completely unburned particles, and 0.8 indicates 20% of the particle mass remains unburned. In the figure, the scaling for the mid-combustor region is changed to focus on the less burned range. Further, these results show that the left-edge of the mid-combustor location ($Y/D = -2.5$) and the right-edge of the near-injector location ($Y/D = 2.5$) have higher mean scattering signal as a result of the elastic wall-scattering.

The centerline-region in both the near-injector and mid-combustor regions, marked by red dotted lines, contains relatively unburned particles in comparison with the peripheral regions

marked using blue dotted lines. Further, these results show that the peripheral return-flow closer to the injector location (and thus also nearer the combustor exhaust) is characterized by higher fuel-conversion efficiency than return flow in the mid-combustor location. As predicted in the previous chapter, the particle burn rate is sufficiently slow that burning continues for most particles as they flow back towards the exit. To further examine the extent of burning of the incoming as well as the return flow, we obtained statistics of the fuel-conversion efficiency corresponding to these centerline and peripheral regions of interest. These specific regions of interest were chosen to minimize the effect of elastic wall – scattering and were held constant corresponding to more than one hundred and fifty different instantaneous images analyzed.

Figure 35 presents the probability density function (PDF s) of local fuel-conversion efficiency and the pixel sample-sizes corresponding to the different regions of interest within both the imaged locations. We begin our analysis based on the statistics of fuel-conversion efficiency from the near-injector location. As evidenced from the results, nearly two – thirds of the pixels show a fuel-conversion efficiency of 25% or less. However there are instances where some parts of the central region of the combustor contain nearly burned packets, characterized by conversion efficiencies higher than 80%. While it is possible that the incoming jet of pet-coke and oxygen occasionally ignites and burns quickly, that is unlikely. It is most likely that the central region included in this analysis is sometimes filled with return flow; in other words, the incoming jet moves away from the central region of interest. However there are instances where some parts of the central region of the combustor contain nearly burned packets (conversion efficiencies of >80%). Similarly, the peripheral – region of the near – injector location usually contains highly burned particles; roughly two – thirds of the pixels in this region show an efficiency greater than 50.0%. Thus the statistics of fuel – conversion efficiency of this region

81

are relatively separated, i.e., somewhat narrow with moderate overlap, at the near − injector heights

Near-Injector
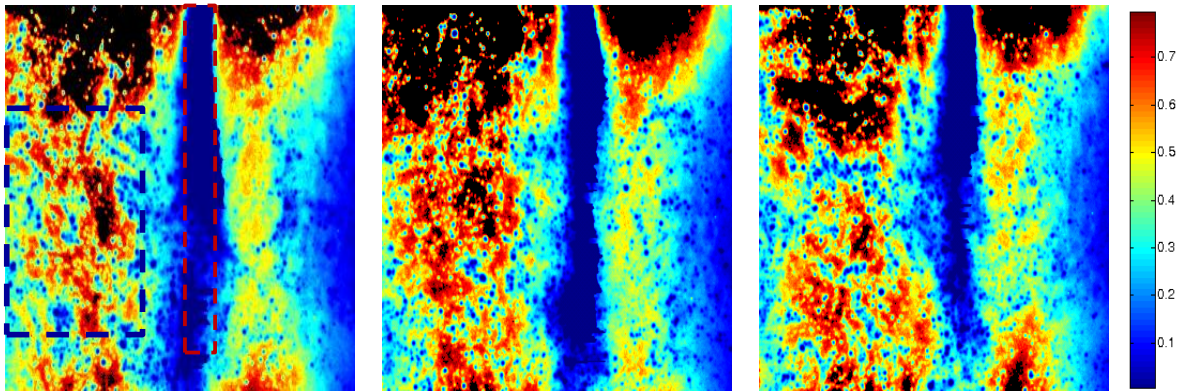
Mid-Combustor
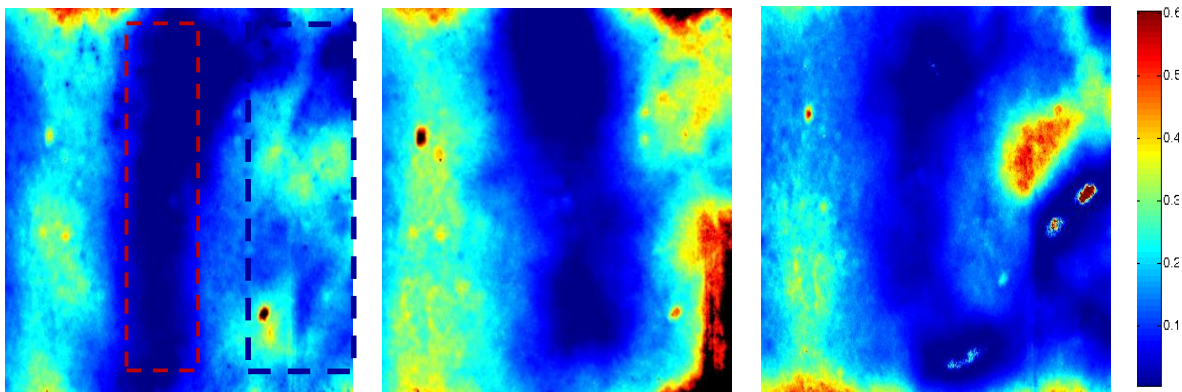
Figure 34. Instantaneous local fuel-conversion efficiency maps obtained from the instantaneous near-injector and mid-combustor particle-scattering images of Figure 2
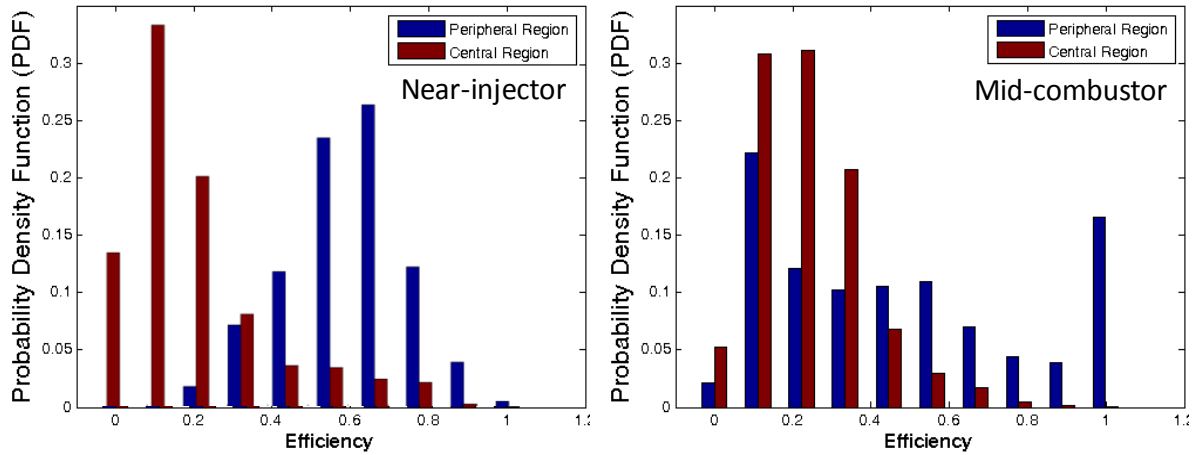
Figure 35. Variation of the statistics of the local fuel-conversion efficiency corresponding to the central and the peripheral regions of the near-injector (left) and mid-combustor (right) imaged locations for the different instantaneous images analyzed

In comparison to the results from the central and peripheral regions of the near-injector location, there is a higher degree of spread as well as overlap of the fuel-conversion statistics between the corresponding regions of interest in the mid-combustor location. Most likely, this is because of the higher degree of lateral movement of the incoming flow in the mid-combustor region, as compared to the near-injector location. Further, as evidenced from the mean-values of the fuel-conversion efficiency, the return flow in the near-injector location represents a higher degree of fuel-conversion than that corresponding to the mid-combustor location.

The analysis of the particle-scattering images has been based on the concept of local fuel-conversion efficiency. However, this is the result of the time history of the flow and thus, not representative of the local heat release rates of these particles. At this point in our discussion, we re-visit concepts in Chapter 2 and Chapter 3 regarding the combustion of solid fuels and the visualization techniques to examine and characterize the local heat – release rates in our combustor.

As described in Chapter 2, the instantaneous volumetric heat-release rates are strongly dependent on the surface reaction rates of individual particles and the number density of the particles. Further, as described in Chapter 2, the surface reaction rates are dependent on the particle temperature and the local oxygen-concentration. As the local luminance signal is related to the emission rate and the number density of the particles, it was shown to be correlated to the local heat-release rates in Chapter 3. The following sub-section analyzes the luminance images acquired simultaneous with the planar particle-scattering images to understand the locations characterized by high heat-release rates. However, as these images capture luminance signal spatially integrated across the width of the combustor, they are less spatially resolved as compared to the planar particle – scattering images presented in this section.

5.1.2 Luminance Images

Similar to the previous section, we begin by analysis of the mean luminance images from the three different regions of the combustor. Figure 36 presents the results of the axial variation of the luminance signal averaged across the width of the combustor. Clearly, the mean-luminance signal from the mid-combustor location is much higher in comparison to that from the near-injector location. Recall from sub-Section 3.1.3.3, the luminance intensity from burning particles is a product of the particle surface area and the particle surface temperature, $A_p T_p^4$. Therefore, the luminance intensity will peak when the particles are only partially burned, i.e., when the surface area and temperature are both high. Thus the fact that the return products are characterized by a higher luminance in the initial mid-combustor location indicates that region can be characterized as an initial burning phase, as compared to the near-injector location, which is characterized by a more final phase of burning.

Next we shift our focus on the instantaneous luminance images acquired from the different locations of the combustor, with typical images presented in Figure 37. As these images capture line-of-sight integrated luminance signal, the central reactant jet is less spatially resolved as compared to the scattering images presented previously. The mid-combustor luminance images reveal the same lateral movement and breakup into reactant packets observed in the corresponding planar particle scattering images. Further, as evidenced from the near-injector images, these product packets burn and leave the combustor on either side of the central injector. In comparison, the near-stagnation location at the bottom of the combustor is characterized by localized regions of relatively low luminance, suggesting either mostly burned particles (low surface area) or low temperatures. Since it is unlikely that the temperature in the bottom section of the combustor is much less than the temperature at the exit, this suggests that the stagnation region at the end of the combustor contains highly burned particles. This is consistent with the stagnation region having long effective residence times. The following section examines the mechanisms that contribute to the ignition of these reactant packets and thus the static stability of the combustion process based on an analysis of the dominant heat feedback mechanisms in the combustor.
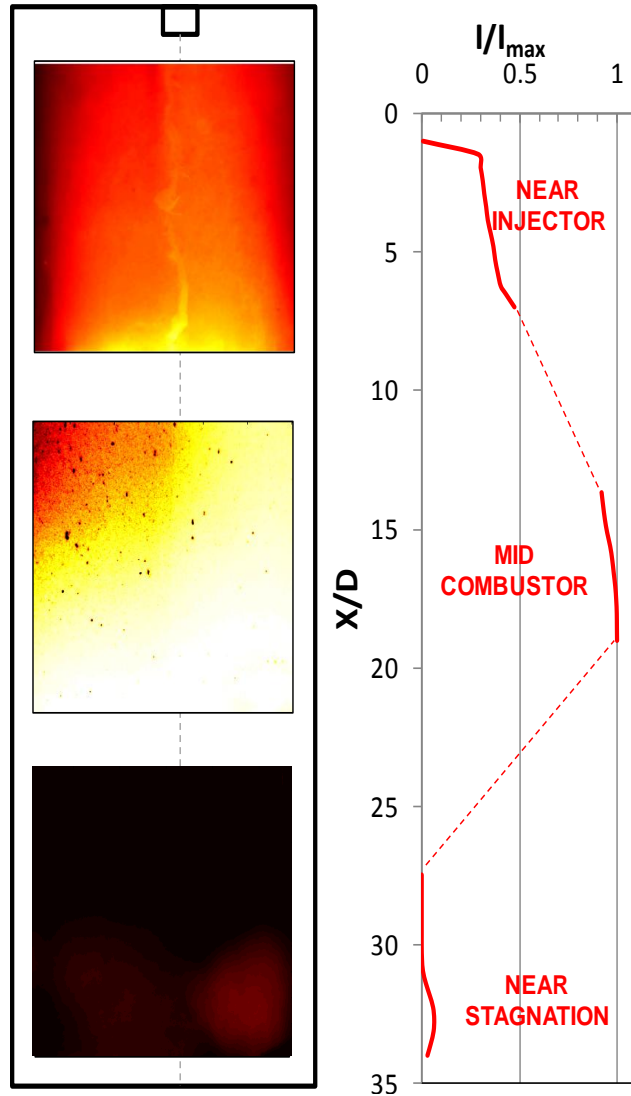
Figure 36. Mean luminance images from the three different imaged locations of the combustor (left) and the variation of the luminance signal integrated across the width of the combustor (right) for the corresponding imaged locations
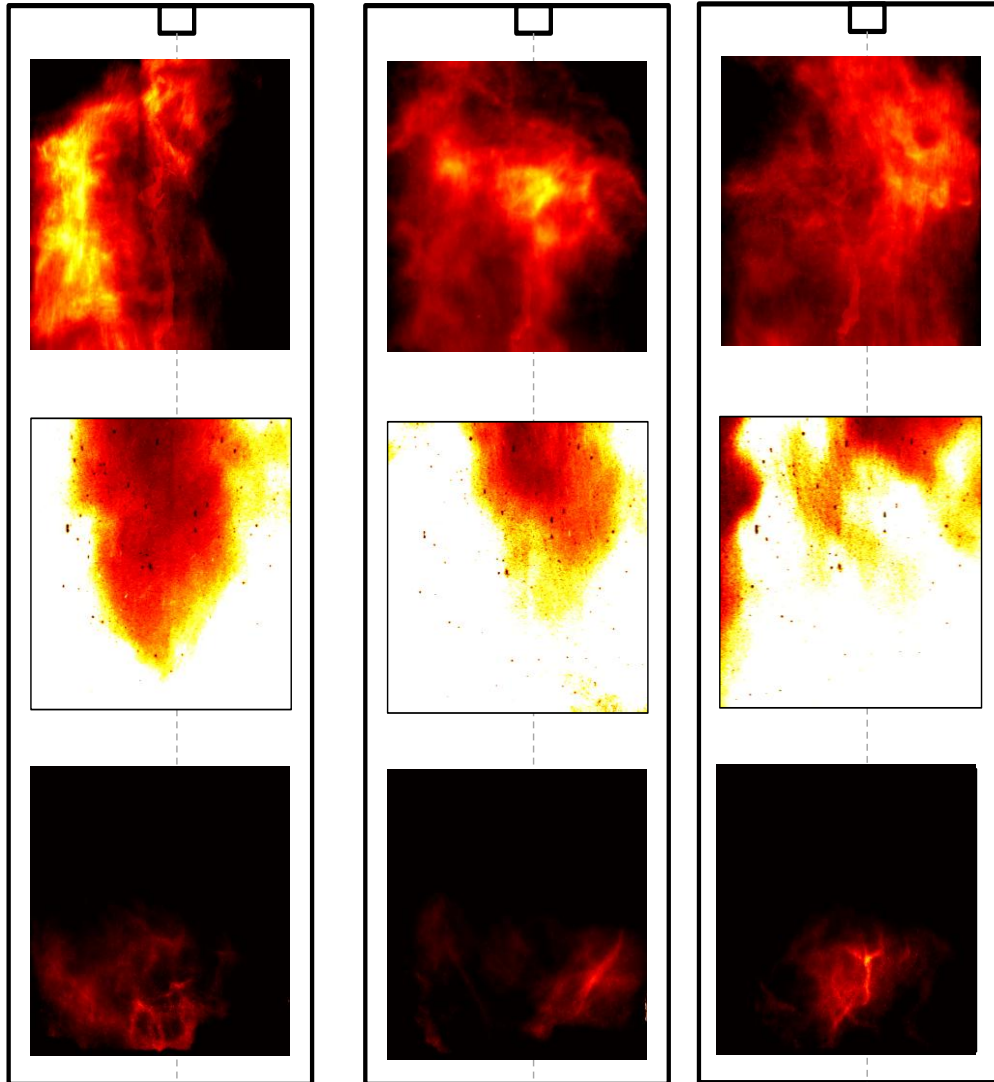
Figure 37. Instantaneous luminance images from the three different imaged locations of the combustor

5.2 Static Stability and Ignition Mechanisms

Practical combustion devices are characterized by high rates of volumetric heat-release, often accomplished using unique geometry and fluid mechanic approaches. The heat-feedback mechanism, unique to the SPRF combustor geometry, transfers heat from the exiting burning products to ignite the reactants, which in turn release heat to sustain the combustion process. Consequently, high rates of volumetric heat-release and efficient heat transfer for ignition are

important factors governing the static-stability of the combustion process. As described in Chapter 2, spatially resolved visualization of the reaction zones revealed that the incoming reactants burned across a highly wrinkled turbulent-flame front in the previous SPRF combustors operating on gas and liquid fuels. Notably, the increased flame surface-area resulted in both higher heat-release as well as heat-transfer (mixing) rates in these combustors. The following sub-section analyzes the corresponding spatially resolved particle-scattering images to understand the dominant mechanisms contributing to static-stability in the solid-fueled SPRF combustor.

5.2.1 Characteristics of Incoming-Jet

As shown in Figure 38, which includes selected scattering images from the near-injector region, the various features exhibited by the incoming jet can be broadly classified into cases where the jet: 1) stays intact, 2) develops localized hot-spots or 3) breaks up into (reactant) packets. Further, it is also evident that the incoming jet displays instances of the break-up behavior corresponding to more than 70% of the total number of instantaneous images analyzed. As reviewed in Chapter 2, the third-quarter of the previous SPRF studies, whose spatial location is roughly coincident with that the mid-combustor location of the current study was characterized by high velocity unsteadiness. This same turbulence production process is likely acting in the current SPRF device in the mid-combustor location and is responsible for the breakup of the incoming jet into reactant packets.
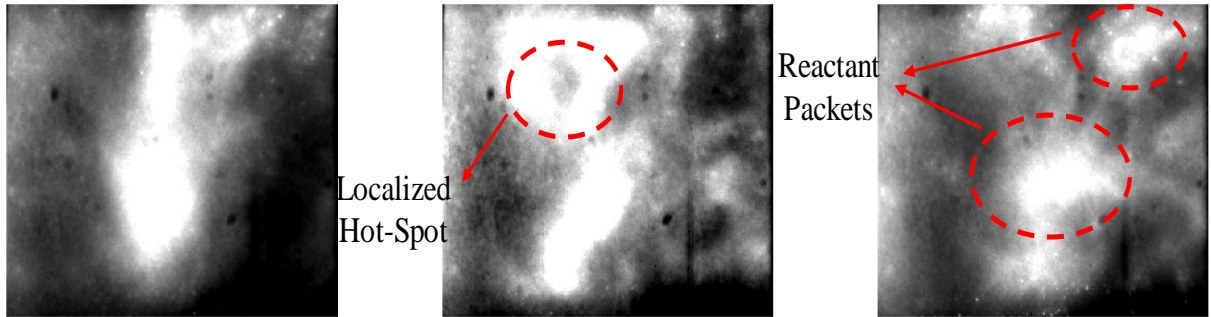
Figure 38. Characteristic behavior exhibited by the incoming reactant jet: jet stays intact (left); jet develops localzed hot-spot (middle) and jet breaks into packets (right)
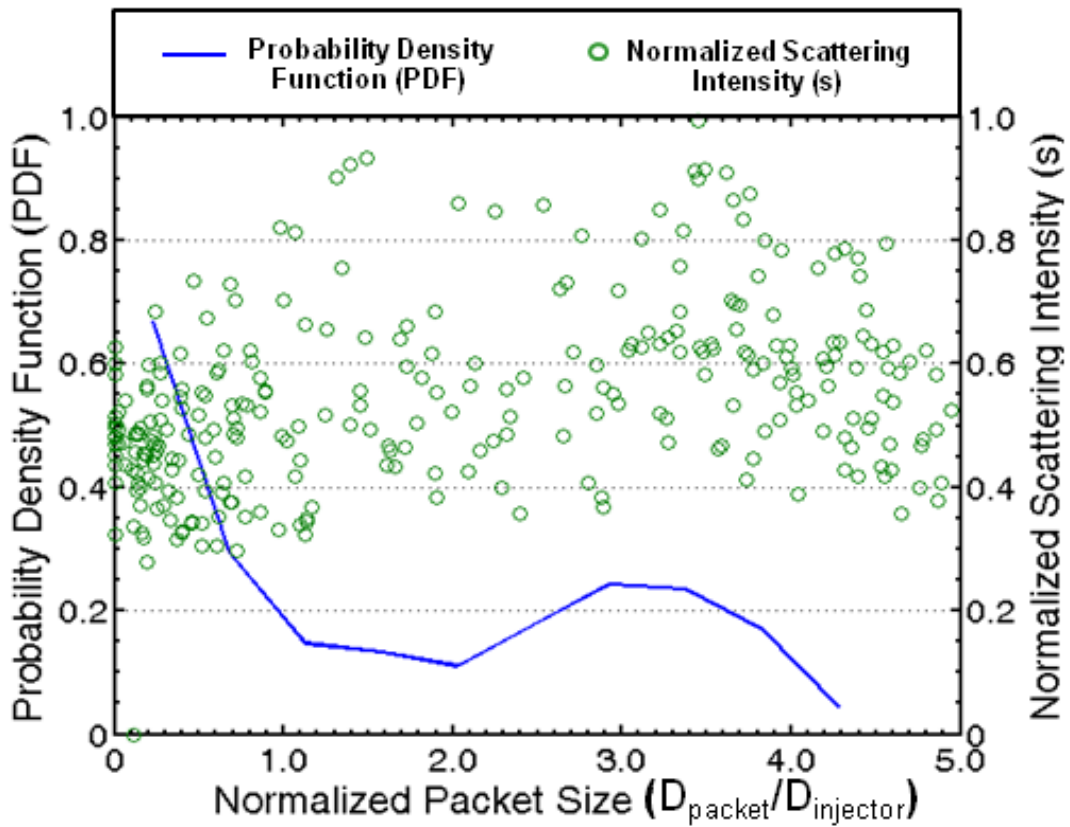
Figure 39. Variation of the statistics of packet size (blue line) and mean scattering signal (green dots) plotted as a function of the normalized packet size

The break-up behavior was further examined based on the analysis of instantaneous images using the intensity threshold technique described in Chapter 3; the results are seen in Figure 39. The packet-sizes have a roughly bi-modal distribution, with the two groups denoted by the terms "small" and "large" packets. The small packets, sized less-than one injector diameter, have comparatively lower particle-scattering signal than the large packets, whose characteristic dimension is between two and four-injector diameters. It is likely that the small packets are sheared off the incoming jet by the burning return products, and partially mixed with the products, resulting in higher proportion of burned matter in the packets. In comparison, the large packets are created due to the large-scale breakup of the mean incoming jet, whose characteristic dimension is comparable to the jet width in the mid-combustor location, e.g., $2.0<W/D<3.0$. Consequently, depending on the history of the breakup-process, these packets are also characterized by a wider distribution of the scattering signal, as compared to the small-sized packets, as seen in Figure 39.

If the small-size packets are mixed with products as indicated above, they could be sufficient hot to auto-ignite and burn. In comparison, depending on the level of preheating/mixing, the particles within the interior of such large packets could auto-ignite from within or ignite from the burning flow at the exterior. The following sub-section examines the combined effect of entrainment and radiative transfer on the preheating of the particles.

5.2.2 Particle Heatup Analysis

In this sub-section, we use the idealized model developed in Chapter 3 to estimate the extent of preheating through the combined effects of radiative transfer as well as product entrainment. The analysis has been performed based on the assumption that the heat feedback occurs close to the injection location, and a heat-feedback location, x_{hf}. Further, it is also assumed that the distribution in agglomerate-size and the incoming velocity can be represented by their representative nominal values. In actuality, the mean flow-field is characterized by spatial variation in the extent of feedback, statistics of agglomerate-size and the incoming velocity. Presumably, at a given axial location, the edges of the incoming jet entrain more burning products and have lower incoming velocity, as compared to the centerline. As a consequence, it is possible to obtain different limits for the variation of predicted preheat temperature based on the corresponding uncertainty limits placed on the nominal model parameters. We restrict our analysis primarily based on uncertainty limits for the mean size, the product fraction level and the incoming velocity. Table 6 provides the various nominal values of parameters used for the study and their corresponding uncertainty limits.

Figure 40 presents the predicted results obtained using the nominal parameters and the possible scatter limits obtained using uncertainty limits on the nominal parameters. In a general sense, the predicted results corresponding to the nominal parameters are representative of the extent of heating within the centerline of the incoming jet. Similarly, the upper limit is characteristic of the corresponding heat up within the shear-layers, characterized by low mean axial velocities and higher levels of product entrainment. Evidently, corresponding to the mid-combustor location, the particles within the shear layers are most likely to auto ignite, in comparison with those at the centerline of the jet.

Table 6. Summary of the various parameters used for the particle heatup model developed in Chapter 3

Parameter	Nominal Value	Uncertainty
$x_{hf}/L_{combustor}$	4.0	-
η_{fuel}	0.58	-
$T_{products}$	2520 K	-
$V_{injection}$	68.0 m/s	±50.0%
f_p	0.8	±50.0%
D_p	98.0 μm	±50.0%

Presumably, the centerline reactant packets have to mix with burning flow before they can ignite. As described in Section 5.1.1, the incoming jet displays a large number of instances of break up into reactant packets. The mixing required for ignition of cold particles within the packets is most likely enhanced as a result of the break up process. Possibly, product entrainment during and enhanced convective transfers after the breakup process are responsible for higher mixing rates between the unburned and the burning flow.
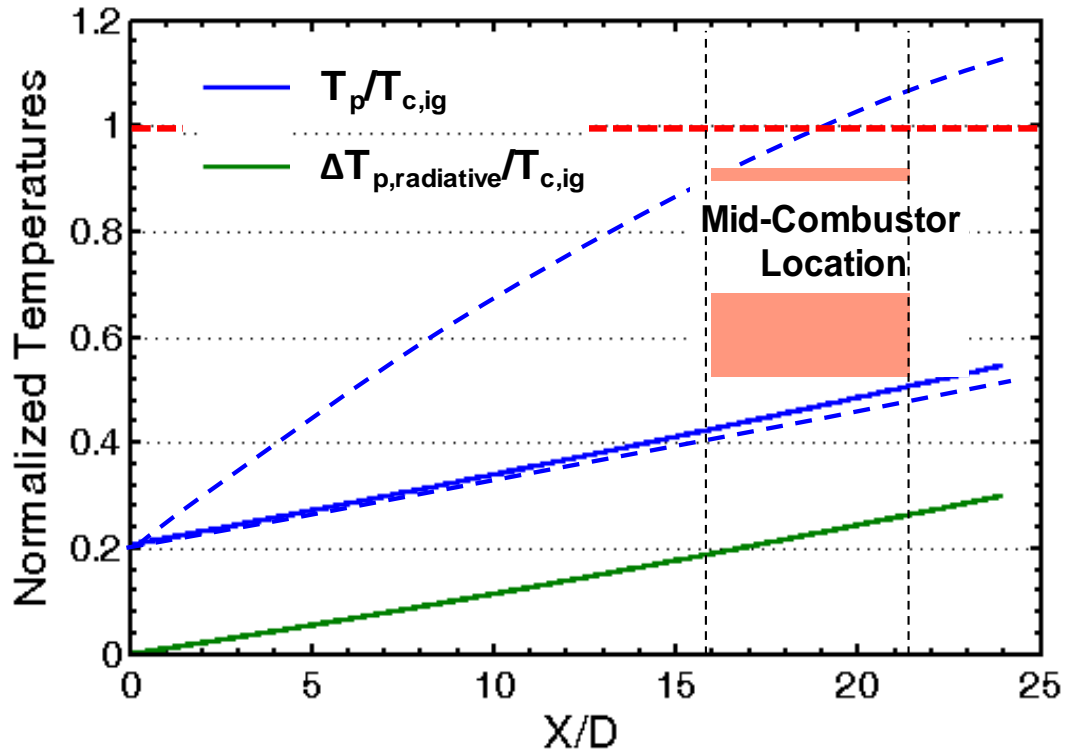
Figure 40. Variation of the normalized predicted particle temperature (blue) as well as the extent of heat-up through radiative transfer, as respective functions of the normalized axial distance.

5.3 Comparison of Combustor Operation

In this section, we compare the SPRF operation on solid-fuels with that of other combustors operating on pulverized coal and air. The specific features of flow-field and combustion processes in the near-field and far-field of the incoming jet are compared, with emphasis on factors contributing to static stability.

5.3.1 Ignition Phase (Near-field)

Visualization studies have been conducted on open, pulverized coal-air flames with methane as the support fuels [36]. Simultaneous planar Mie-scattering and OH- laser induced

fluorescence techniques were used to identify the spatial location of particles in relation to the heat-release. These studies proved that significant heat-release occurred at the edges of the jet, away from the regions characterized by high scattering signal. As a consequence, the authors concluded that the reaction zones had a character of a non-premixed gas flame supported by devolatilization from the particles. In comparison to coal, petroleum-coke has lower volatile content. Presumably, the heat-release in the ignition phase is entirely due to surface reactions and thus different from the volatile flame mechanism.

5.3.2   Quasi-steady combustion phase (Far-field)

Experimental video images of swirling pulverized coal-flames reveal typical sinuous features in the far-field of the incoming jet, resulting in overall increase in the flame-area [37]. These studies also reported LES simulations of incident radiant emission superimposed on the video images show. As the experimentally observed features show good agreement with the predicted results, the authors concluded that LES simulations provide reliable information on the actual flow-field and combustion processes of swirling coal flames. Based on the planar instantaneous LES results, the authors also concluded that the in the far-field of the jet, the heat-release occurs due to char combustion. Further, as reported by the authors, the high heat-release rates in the far-field results in the sinuous features mentioned previously, although the incoming jet remained continuous.

In comparison to the sinuous, yet continuous far-field jets characteristic of swirling coal-flames, the incoming jet in our combustor exhibits breakup behavior. Presumably, this is the result of higher unsteadiness levels as a result of higher heat-release and thus dilatation rates in our combustor.

5.4   Concluding Remarks

Visualization studies on the reacting flow-field of the SPRF combustor operating on a solid-fuel like pet-coke have shown that most of the heat-release occurs in the mid-combustor location. Corresponding to this location, the incoming jet displays prominent characteristics of break-up into reactant packets predominantly of two size distribution. This is unlike the behavior in pulverized coal-air jet flames, where the near-field of the jet has the character of a detached volatile flame and the far-field jet is predominantly continuous with sinuous features.

The bimodality of packet-size distribution is suggestive of two distinct mechanisms of breakup, namely the shear breakup and the large-scale breakup. The former mechanism is the result of the burning return flow shearing the incoming jet into small-sized packets, while the latter occurs due to large-scale break-up of the incoming jet into larger packets as a result of the unsteady velocity field. Predictions using idealized model of particle heating suggests that the large-packets must break-up and mix with burning products prior to ignition. The dynamics of these large packets can be studied by tracking them using high-speed imaging.

CHAPTER 6

CONCLUSIONS AND RECOMMENDATIONS FOR FUTURE WORK

6.1   Summary and Conclusions

This thesis investigated the performance of the central injection SPRF geometry scaled to operate on low-grade solid fuels. The scaling was based on the previous SPRF studies. Preliminary testing has demonstrated that the combustor operates stably on pure-oxygen and a slurry made from petroleum-coke and water at a baseline operating condition, defined based on operating power. The fuel-conversion efficiency remained relatively unaffected within a range of variations in mean particle-size and water-content in the slurry. Similarly, the performance was also found to be unaffected corresponding to off-baseline conditions characterized by higher operating power. Thus the SPRF geometry has been demonstrated to be a robust combustor concept for burning low-grade fuels.

An idealized model for quasi-steady burning has been developed for the SPRF combustor based on estimates of parameters like residence time, heat-losses and mixture composition. The model predictions have been found to agree reasonably with the measured values within the limit of errors due to parameter uncertainties. In a separate series of simulations, the model predicted complete fuel-conversion corresponding to operating conditions like higher pressure and lowered heat-losses. Thus it has been possible to examine the effect of future design changes on the performance of the scaled SPRF combustor.

Visualization studies have been conducted on an optically accessible version of the scaled SPRF combustor to study the flow-field. With the use of techniques like planar particle-scattering and luminance imaging, these studies have shown that ignition and intense burning occurs in the mid-combustor location, with the incoming jet displaying predominant breakup

behavior. The broken packets are characterized by a bimodal size distribution, suggestive of two dominant mechanisms of breakup. The smaller sized packets, characterized by lower scattering signal and thus higher proportion of burning matter, are sheared off the main jet by the return flow. In comparison, the bigger packets are the result of the large scale breakup of the incoming flow as a result of the highly unsteady velocity field. Analogous to the breakup of large scale vortical structures, these larger packets could break up into smaller packets and mix with the ambient burning flow.

Predictions of the idealized model of particle heat-up rule out the likelihood of auto-ignition of individual particles within the center of these packets. However, it is possible for the corresponding particles in the edges to ignite through sufficient mixing with the burning return flow. The mixing process required for the ignition of the colder particles within the interior of these packets occurs during the breakup of these packets or during convective transfer of burning flow from the exterior.

6.2   Main Contributions

6.2.1   Pet-coke Combustion: Robust Flame Holding

The main contribution of this work is the result of studies that conclusively proved that the SPRF geometry is a robust flame-holding concept for operation on low-grade solid-fuels, specifically petroleum-coke. The prototype combustor has been shown to operate stably corresponding to different conditions without superior support fuels or external reactant preheating. These results are compared against those of previous studies on pet-coke slurry in twin-atomizer quarl-burners. Unlike our prototype combustor, statically stable operation was not possible without superior support fuels for the quarl-burner studies mentioned previously.

Further, the power density of our prototype combustor was much higher than the quarl-burner, i.e. order of MW/m^3, as compared to kW/m^3.

6.2.2 Solid-Fueled Operation: Combustor Physics

An equally significant contribution of this work is the result of visualization studies on the solid-fueled SPRF combustor compared against that of pulverized coal-air jet flames. These studies have helped to understand the differences between the mechanism of SPRF combustor operation and that of pulverized coal-air jet flames. While the near-field of these jet flames has the character of a typical volatile flame, the far-field behavior is significantly different. In the far-field regions, the high heat-release associated with char-combustion results in the continuous jet exhibiting prominent sinuous features. In comparison, the heat-release rates and thus the unsteadiness levels are higher in our SPRF combustor, resulting in the breakup of the incoming jet. As a consequence, the extent of mixing and entrainment of the incoming reactants with the burning products is significantly enhanced. Presumably, this unique mechanism is responsible for the statically stable SPRF combustor operation with petroleum-coke which is characterized by significantly lower volatile content than coal.

6.3   Recommendations for Future Work

Although this thesis provides the basis for a thorough understanding of the operation of the scaled SPRF geometry on low-grade solid fuels, many aspects of the performance still need to be studied further. This section deals with the three main aspects of the aforementioned performance, namely the static stability mechanism, design modifications and the various practical applications.

The planar visualization studies showed the incoming jet breaking into packets characterized by different levels of mixing. However, the eventual fate of these packets was

98

postulated based on predictions of the idealized model of particle heat up. These theories need to be validated based on tracking of packets using a high-speed imaging system. Further, it would also be possible to characterize the flow-field and compare it with that of the gas-fueled SPRF combustor, normalized based on volumetric power densities. This would enable the investigation of the effect of heat release rates on the general unsteadiness in the SPRF combustor operating on various fuels.

The scaled SPRF geometry also needs modifications to improve the performance. As most of the heat release occurs in the mid-combustor region, it should be possible to reduce the combustor length without affecting the combustor flow-field and mixing characteristics. This modified shorter version can be built with superior refractory walls would reduce the heat losses and thus result in improved fuel-conversion efficiency.

One potential application of this SPRF device is pulverized coal furnaces involving operation on air or enriched air. As the scaled SPRF combustor showed good performance corresponding to high levels of dilution, self-sustained operation would be possible with low levels of external preheating. Another application is high-pressure steam generation involving direct injection of water into the combustion products. However, at higher operating pressures, injector pressure drop restricts typical injection velocity and thus the quality of atomization.. Similar to the previous application, external preheating of the incoming flow may also be needed to ensure statically stable operation.

REFERENCES

1. Turns,S., *An Introduction to Combustion: Concepts and Applications*, McGraw-Hill, 2000.

2. Cho, S.Y., Yetter, R. A., and Dryer F. L., *A Computer Model for One-Dimensional Mass and Energy Transport in and around Chemically Reacting Particles, Including Complex Gas-Phase Chemistry, Multicomponent Molecular Diffusion, Surface Evaporation, and Heterogeneous Reaction.* Journal of Computatioanal Physics, 1992. 102: p. 160-179.

3. H., H.R., *Structure, properties and reactivity of solid fuels.* Proceedings of the Combustion Institute, 1998. 27: p. 2887-2904.

4. Yamamoto, K., *Biomass Power Generation by CFB Boiler.* NKK TECHNICAL REPORT-JAPANESE EDITION-, 2001: p. 22-26.

5. Beer J.M, C.N.A., *Combustion Aerodynamics.* 1983: Krieger.

6. Suda T., T.M., Hirata T., Yoshino M., Sato J. *A Study of Combustion Behavior of Pulverized Coal in High Temperature Air* in *Proceedings of the Combustion Institute.* 2002.

7. Heil P., T.D., Stadler H., Tschunko S., Forster M., Kneer R., *Development of an oxy-coal swirl burner operating at low O_2 concentrations.* Fuel, 2009. 88: p. 1269-1274.

8. Feihu Li , J.Z., Xiaoru Fu , and Guanghong Sheng, *Characterization of Fly Ashes from Circulating Fluidized Bed Combustion (CFBC) Boilers Cofiring Coal and Petroleum Coke.* Energy and Fuels, 2006. 20(4): p. 1411-1417.

9. C.M.H. Brereton, C.J.L., J.R. Grace, A. Luckos, J. Zhu, *Pitch and coke combustion in a circulating fluidized bed.* Fuel, October, 1995. 74(10): p. 1415-1423.

10. Jinsheng Wang, E.J.A., Juan Carlos Abanades, *Clean and efficient use of petroleum coke for combustion and power generation.* Fuel, 2004. 83(10): p. 1341-1348.

11. Jihui Chen, X.L., *Progress of petroleum coke combusting in circulating fluidized bed boilers-A review and future perspectives.* Resources,Conservation and Recycling, 2007. 49(3): p. 203-216.

12. Y. Neumeier, J.M.C., Y. Weksler, B.T. Zinn, J. Seitzman, J. Jagoda, J. kenny, *Ultra Low Emissions Combustor with Non-Premixed Reactants Injection*, in *41st AIAA/ASME/SAE/ASEE Joint Propulsion Conference* 2005: Tucson, AZ.

13. Bobba, M., et al. *Flame stabilization and mixing studies in a novel ultra-low emissions combustor.*

14. Haynes, H. and N.P. Council, *Enhanced Oil Recovery: An analysis of the potential for enhanced oil recovery from known fields in the United States, 1976-2000.* 1976.

15. Speight, J.G., *The chemistry and technology of petroleum.* Vol. 114. 2007: CRC.

16. Grinzi F., R.G. *Combustion Trials on Coal Water Slurry and Petroleum Coke Water Slurry.* in *Proc. 7th Intl. Symposium on Coal Slurry Fuels Preparation and Utilisation*. May 1985. New Orleans, U.S.A.

17. Gopalakrishnan, P., *Measurements and modeling of the flow field in an ultra-low emissions combustor*, *AIAA-2006-0962* in *44th AIAA Aerospace Sciences Meeting*. 2006.

18. Gopalakrishnan, P., M.K. Bobba, and J.M. Seitzman, *Controlling mechanisms for low NOx emissions in a non-premixed stagnation point reverse flow combustor.* Proceedings of the Combustion Institute, 2007. 31: p. 3401-3408.

19. Gopalakrishnan, P., *Effects of the reacting flowfield on combustion processes in a Stagnation Point Reverse Flow combustor*, in *Aerospace Engineering*. 2008, Georgia Institute of Technology: Atlanta.

20. M.K. Bobba, P.Gopalakrishnan, J.M. Seitzman and B.T. Zinn. *Characterisitcs of Combustion Processes in a Stagnation Point Reverse Flow Combustor", GT2006-91217.* in *Proceedings of the ASME/IGTI Turbo Expo May 2006*. 2006. Barcelona, Spain.

21. P. Gopalakrishnan, J.S., Y. Neumeier, A. Radhakrishnan. *Characterization of the Reacting Flowfield in a Liquid-Fueled Stagnation Point Reverse Flow Combustor -AIAA-2007-0172.* in *45th Aerospace Sciences Meeting* 2007. Reno, NV.

22. Bobba, M.K., et al. *Flame structure and stabilization mechanisms in a stagnation point reverse flow combustor - GT2007-28231.* in *Proceedings of the ASME/IGTI Turbo Expo 2007*. 2007. Montreal, Canada. : ASME.

23. I. Glassman, R.A.Y., *Combustion.* 2008: Elsevier.

24. Krazinski, J.L., R.O. Buckius, and H. Krier, *Coal dust flames: A review and development of a model for flame propagation.* Progress in Energy and Combustion science, 1979. 5(1): p. 31-71.

25. Huang, Y., et al., *Combustion of bimodal nano/micron-sized aluminum particle dust in air.* Proceedings of the Combustion Institute, 2007. 31: p. 2001-2009.

26. Boukara, R., et al. *Study of the ignition of single coal and char particles in a drop tube furnace by a probability method*. 1992: Elsevier.
27. Young, B.C. and I.W. Smith, *The kinetics of combustion of petroleum coke particles at 1000 to 1800 K: The reaction order.* Symposium (International) on Combustion, 1981. 18(1): p. 1249-1255.

28. Smith G.P., G.D.M., Frenklach M.,Moriarty N.W., Eiteneer B., Goldenberg M., Bowman C.T., Hanson R.K., Song S., Gardiner Jr. W.C., Lissianski V., and Qin Z., . www.me.berkeley.edu/gri_mech/. . GRI-Mech homepage,Gas Research Institute 1999.

29. Ghosh, B., Basu, D. and Roy, N. K., , *Studies of Pulverized Coal Flames*, in *Sixth Symposium (International) on Combustion*. 1956: Reinhold, New York.

30. Horton, M.D., Goodson, F. P. and Smoot, L.D.,, *Characteristics of Flat, Laminar Coal Dust Flames*. Combustion and flame, 1977. 28: p. 187-195.

31. H. Schneider, C.P., *Determination of turbulent burning velocities of dust air mixture with the open tube method*. Journal of Loss Prevention in Process Industries, 2006. 20: p. 470-476.

32. Bobba, M., *Product recirculation and mixing studies in a stagnation point reverse flow combustor - AIAA-2007-0173*. in *45th Aerospace Sciences Meeting*. 2007. Reno, NV.

33. G.J. Germane, L.D.S., S.P. Diehl, K.H. Richardson, D.C. Rawlins. in *Fifth International Symposium on Coal Slurry Combustion and Technology*. 1983. Pittsburgh Energy Technology Center, Pittsburgh.

34. Rand Thurgood, J., L. Douglas Smoot, and P.O. Hedman, *Rate Measurements in a Laboratory-Scale Pulverized Coal Combustor*. Combustion Science and Technology, 1980. 21(5-6): p. 213-223.

35. R. Morrell, J.S., M. Wilensky, J. Lee, E. Lubarsky, B. Zinn. *Interpretation of Optical Flame Emissions for Sensors in Liquid-Fueled Combustors, AIAA-2001-0787* in *39th AIAA Aerospace Sciences Meeting*. 2001. Reno, NV.

36. Seung min Hwang, R.K., Fumikeru Akamatsu, Hirofumi Tsuji, Hisao Makino and Masashi Katsuki, *Application of Optical Diagnostics Technique to a Laboratory-Scale Turbulent Pulverized Coal Flame*. Energy and Fuels, 2005. 19: p. 382-392.

37. P. Edge, S.R.G., L. Ma, R. Porter, M. Pourkashanian, A. Williams. *LES modelling of air and oxy-fuel pulverised coal combustion—impact on flame properties*. in *Proceedings of the Combustion Institute 33*. 2011.